Present-day crustal vertical velocity field for the Contiguous United States

Nicholas Lau[1], Adrian A. Borsa[1], Thorsten W. Becker[2,3]

[1]Scripps Institution of Oceanography, University of California San Diego, La Jolla, CA, USA
[2]Institute for Geophysics, Jackson School of Geosciences, The University of Texas at Austin, Austin, TX, USA
[3]Department of Geological Sciences, Jackson School of Geosciences, The University of Texas at Austin, Austin, TX, USA

Key Points:

- GPS vertical velocity field of CONUS reflects tectonics, surface mass loading, and isostatic rebound.
- Residual velocities may reflect Earth's center of mass translation motion.
- Removing GIA model predictions and GRACE-derived hydrologic loading reduce velocity field variance by 36%.

Corresponding author: Nicholas Lau, `h4lau@ucsd.edu`

Abstract

The study of vertical crustal motion in the contiguous United States (CONUS) has traditionally focused on the high amplitude deformation caused by glacial isostatic adjustment. To better understand more subtle vertical crustal motion resulting from other geophysical processes, we take advantage of the ongoing expansion of continuous Global Positioning System (GPS) networks, whose geodetic observations provide ever-increasing accuracy and spatial resolution of surface deformation. Using position data for 2782 GPS stations operating between 2007 and 2017, we produce a new vertical crustal velocity field for the CONUS region. We estimate our own station velocities to ensure consistent treatment of time series outliers, noise, and offsets, and we use adaptive smoothing and interpolation to account for spatially varying station density. Our velocity field reveals spatially coherent vertical features that are representative of regional tectonics, hydrologic, and anthropogenic processes. By removing the effects of modeled glacial isostatic adjustment and hydrologic loading estimated from Gravity Recovery and Climate Experiment (GRACE) data, we reduce the variance in our velocity field by 36% and show residuals potentially due to geocenter motion and underlying tectonics.

1 Introduction

Direct measurements of crustal motion using satellite geodetic techniques have vastly improved our understanding of fundamental solid Earth processes. The Global Positioning System (GPS) has been a cornerstone of current geodetic studies, providing continuous observations of crustal motion over the past two decades. In the contiguous United States (CONUS), where station distribution is relatively dense and temporal coverage extends a decade or longer, horizontal GPS position measurements are frequently used in plate boundary deformation applications such as earthquake fault slip distribution (e.g. Jónsson et al., 2002; Fialko, 2004), interseismic strain accumulation (e.g. J. R. Murray et al., 2001; Kreemer et al., 2014), and tectonic block modeling (e.g. Bennett et al., 2003; Meade & Hager, 2005; Becker et al., 2005; Hammond et al., 2011). To fully quantify three-dimensional crustal deformation, there has been recent increased attention to vertical GPS data. The vertical component of GPS has traditionally been treated with caution due to its low signal-to-noise ratio relative to horizontal components, whose uncertainties are 2−3 times lower than those of the verticals. It typically requires more than 5 years of continuous data to achieve 1σ uncertainty levels of under 1 mm/yr, (Williams et al., 2004; Santamaría-Gómez et al., 2011; Bock & Melgar, 2016) and for seasonal effects to have a negligible impact on velocity estimation (Blewitt & Lavallée, 2002). As a result of the massive deployment of high-quality permanent GPS stations in CONUS during the mid-early 2000s as part of the Plate Boundary Observatory (PBO) network (Herring et al., 2016), there is now broad coverage of GPS across CONUS that spans over a decade, enabling robust measurements of vertical crustal motion at different spatial scales.

Glacial isostatic adjustment (GIA) has long been recognized as one of the long-term drivers of current vertical deformation in North America and has produced observable signals in various geodetic records with a footprint extending across the entire CONUS (Peltier, 1996; Davis & Mitrovica, 1996; Sella et al., 2007; van der Wal et al., 2008). While the high latitudes of North America are experiencing post-glacial uplift from the deglaciation of the Laurentide, Cordilleran, and Innuitian ice sheets, GIA in CONUS primarily reflects the flexural forebulge's adjustment to the northward retreat of ice sheet, resulting in downward motion as observed in early GPS measurements (Park et al., 2002; Calais et al., 2006; Sella et al., 2007). Several recent studies have utilized GPS velocities to construct vertical velocity fields over most or all of CONUS (Snay et al., 2016; Kreemer et al., 2018; Husson et al., 2018). These studies, which map and interpolate GPS station velocities, agree that GIA is a major mechanism for continental-scale vertical deformation, and they similarly define the spatial extent of subsidence from the collapse of the forebulge. Joint analysis of horizontal strain rates and vertical displacement rates provides additional constraints on the physical mechanisms of the underlying observed GIA (Kreemer et al., 2018). While earlier methods of constraining vertical motion provided insight into the longer wavelength nature of GIA, the increased spatial resolution obtained by recent velocity fields reveals the presence of shorter wavelength variations, indicating other sources of deformation should be considered in understanding current vertical crustal motion in CONUS.

We recognize the potential importance of these features and make a case below for the need to expand upon the past study of vertical deformation motivated for several reasons. The recent emergence of studies on crustal elastic response to hydrologic loading shows that significant crustal deformation can be observed in GPS observations at local to continental scales (Borsa et al., 2014; Amos et al., 2014; Argus et al., 2017; Adusumilli et al., 2019). Separately, given the complex tectonic history of the North American plate and its active deformation along the Pacific plate boundary, it is imperative to see whether tectonic features of different spatial scales can be resolved by current geodetic observations. There are also questions raised about potential links between mantle convection, surface topography, and seismicity that can potentially be studied by joint geodesy-geodynamics analysis (e.g. Becker et al., 2015). Moreover, improved spatial estimates of vertical land motion along the coast can augment other observational methods, such as tide gauges, in understanding relative sea level change, which is an increasingly important issue to coastal communities (e.g. Wöppelmann & Marcos, 2016; Hawkins et al., 2019).

We therefore focus this study on vertical crustal deformation in CONUS, with three main objectives in mind. The first objective is to create a GPS-derived vertical velocity field that can spatially resolve non-GIA deformation processes. To this end, we produce a GPS-derived gridded vertical velocity field that reflects decadal trends from 2007 to 2017, adapts spatial resolution to match GPS station density, features smooth spatial derivatives, and is robust to outliers. The second objective is to understand solid Earth processes such as tectonics, elastic loading, anthropogenic, and mantle dynamics that are currently observable in the vertical velocity field at regional to continental wavelengths, and to assess whether they are representative of long-term crustal motion. The last objective is to assess whether interpretation of vertical crustal velocities over CONUS is improved by removing contributions from modeled GIA and hydrologic loading.

2 Data

2.1 GPS

To investigate long-term deformation in the CONUS region, we analyzed 'up' position time series for 2782 GPS stations located within the 22^o N/52^o N and -130^o E/-65^o E boundary, restricting our analysis to time series that span at least 6 years between 2007 and 2017. Setting the minimum time series length to 6 years ensures that estimated velocities are minimally biased from least-squares velocity estimation or due to any uncorrected annual or semi-annual sinusoidal signals (Blewitt & Lavallée, 2002). To better observe solid Earth processes, we omitted stations that are known to be dominated by poroelastic effects. This include all stations within California's Central Valley, where water extraction results in volumetric changes in groundwater aquifers and accompanying surface subsidence (K. D. Murray & Lohman, 2018; Neely et al., 2020).

GPS data were taken from the Nevada Geodetic Laboratory (NGL) at the University of Nevada (UNR), where daily positions in the IGS08 reference frame were processed using Jet Propulsion Laboratory's GIPSY-OASIS-II software (Blewitt et al., 2018). NGL processes GPS RINEX files collected by numerous individual operators, ranging from academic research networks to state agency surveying networks. These networks provide coverage over different regions, such as EarthScope's Plate Boundary Observatory in the western United States, NOAA's Continuously Operating Reference Station across CONUS, and California statewide coverage by its Department of Transportation. While there are publicly available GPS position time series from other analysis centers, we choose to use

UNR's solution because it includes the largest number of GPS station, all processed using the same procedures and the same standards.

For each GPS station, we obtain a "seasonally adjusted" position time series by estimating and removing seasonal motion using the STL algorithm (seasonal-trend decomposition using LOESS; Cleveland et al., 1990). STL decomposes a time series into trend, seasonal, and residual components by a combination of lowpass filtering and fitting local polynomials to seasonal cycles in the data. This method is preferred over fitting single or double sinusoids as it better captures temporal asymmetry in seasonal cycles. We then correct for step-like offsets in these seasonally adjusted time series. Offsets in GPS time series, caused by coseismic displacements, equipment changes, or unknown reasons, are known to bias secular velocity estimation (Williams et al., 2004; Gazeaux et al., 2013). NGL provides a list of offset dates due to equipment changes and coseismic displacements that can be used for offset estimation and removal, however we found some undocumented offsets in the UNR time series. To mitigate potential problems from undocumented offsets, we use a cumulative sum control chart (CUSUM) sequential analysis-based algorithm that automatically detects and estimates offsets locally (supplementary materials; Page, 1954) instead of using provided dates. This method enables detection of all offsets without relying on external information. Fitting offset in a local basis also does not require a specific function to fit the entire time series.

Finally, we estimated vertical velocities by applying robust least-squares linear regression to the offset-corrected and seasonally adjusted GPS time series (Figure 1). Although UNR and other analysis centers publish their own velocities, our procedure employs seasonal corrections which we think are more realistic, ensures that all offsets are detected and corrected, and imposes tighter temporal constraints on GPS data in order to ensure the measured deformation is representative of a fixed time period.

2.2 Glacial Isostatic Adjustment

In this study, we consider 3 published models to constrain the GIA contribution to vertical motion: ICE-5G VM2 (Peltier, 2004), ICE-6G_D VM5a (Peltier et al., 2018), and Caron (Caron et al., 2018). Various sets of observational constraints, such as geologic record of the ice sheet margin, local geologic record of relative sea level, and contemporary GPS rates are used in these the models, in addition to the different ice loading histories. The ICE-5G and ICE6G_D models use an iterative inversion approach that minimizes misfit to observational constraints by varying ice loading geometry and history, while keeping the viscosity structure fixed. Caron et al. on the other hand employs a Bayesian statistics method using large number of forward models computed with vary-

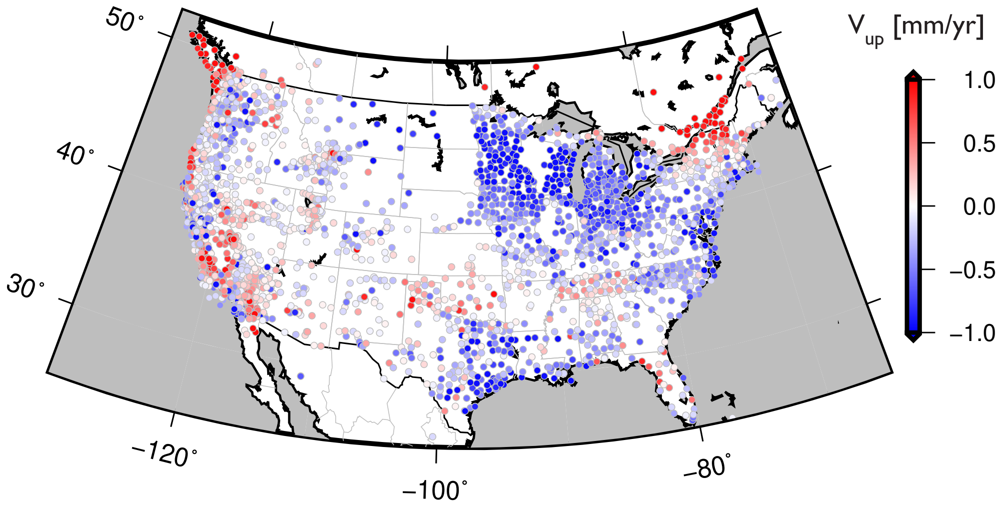

Figure 1. GPS stations used in this study.

ing rheological parameters, elastic lithospheric thickness, and ice loading history. All of the models are expressed in the same center of mass reference frame as GPS, allowing us to directly compare model predictions of surface displacements to our GPS velocity estimates.

2.3 Hydrological Loading

To estimate the contribution to the CONUS vertical velocity field from hydrology, we modeled elastic surface vertical displacement rates due to mass loading from fluctuations in CONUS terrestrial water storage (TWS). We considered using TWS from relevant parameters of the daily National Land Data Assimilation System (NLDAS) NOAH model. However, NLDAS does not fully capture interannual TWS variability from large well-documented storage anomalies (e.g. the California drought of 2013-2016 Argus, Fu, & Landerer, 2014). We instead used TWS estimates from NASA's GRACE satellite gravity mission, which captures long-term water storage variability, albeit at reduced temporal (1 month) and spatial ($\sim$ 300 $-$ 400 km) resolution. While we considered mascon solutions from the German Research Centre for Geoscience (GFZ), Jet Propulsion Laboratory (JPL), Goddard Space Flight Center (GSFC), and Center for Space Research (CSR), we ultimately choose the Center for Space Research's RL06 mascon solution (Save et al., 2016) mainly since it deviates the least from the mean of the 4 solutions. The CSR solution includes degree-1 geocenter corrections, has its C_{20} coefficients replaced by satellite laser ranging data, and is corrected for GIA with ICE-6G_D. We then forward modeled vertical displacements due to GRACE-estimated TWS using the SPOTL package (Agnew, 1997), which computes the solid Earth elastic response to surface mass loading by convolving the load with elastic Green's function for the Gutenberg-Bullen Model A Earth reference model (Farrell, 1972).

3 Methods

3.1 Interpolation and gridding of GPS velocities

Since GPS station distribution varies across CONUS, we created an interpolation method that adapts the spatial resolution of the vertical velocity model to variations in station density, allowing us to capture higher levels of detail where supported by the data. This method contains two main steps: 1) block median and 2) adaptive radius smoothing.

For step one, we first apply a 0.25-degree block median filter to downweight the influence of dense clusters of stations that reflect mostly local effects, such as the > 40 stations located within one-degree distance of the Long Valley Caldera. The block median computes the median and the centroid location of all stations within each grid cell, which are then used as the single datum for the grid cell (Figure S1). For grid cells with multiple stations, this step dampens outliers while retaining the common, dominant signal. The quantity w is computed for each grid cell by finding its median distance to the closest N -centroids (see Section 3.2 on the choice of the N).

Step two is to smooth results obtained from the previous step with an adaptive radius Gaussian kernel. Since empty grid cells can cause input data to be unevenly weighted by the kernel, we populate remaining empty grid cells from step one using nearest neighbor interpolation prior to applying the kernel. The radial kernel, with weights of $\exp(-r^2/w^2)$, is then convolved with the grid cells. The width of the kernel w varies based on GPS station density, hence yielding higher resolution in areas with more stations (Figure S2). To limit influence of extreme far field grids, a maximum threshold of 300 km is set for r.

3.2 Testing and validation of modeling approach

We perform synthetic checkerboard tests to validate the resolution of our interpolation. We follow the methods described above in Section 3.1 to create velocity models from 2.5 and 5-degree synthetic checkerboards (uniform latitude/longitude with alternating values of 1 and -1), sampled at actual GPS station locations. Figure 2 shows output of 2.5 and 5-degree checkerboard test. The 5-degree input grids are well resolved in

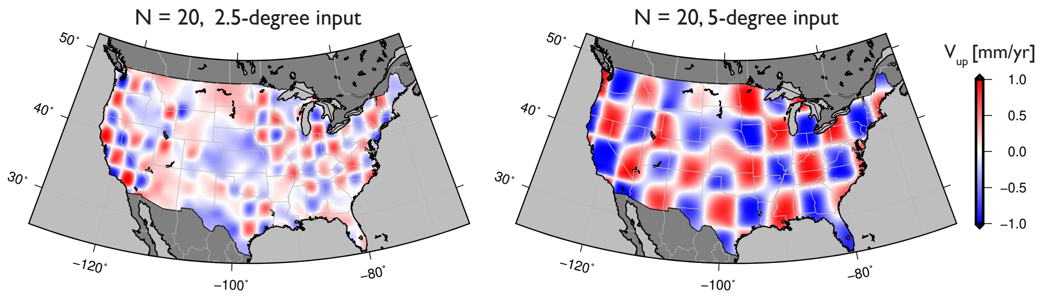

Figure 2. Checkerboard test for GPS interpolation resolution using $N = 20$ centroids, with input checkers of 2.5-degree (left) and 5-degree (right) grids.

most regions, with the checkerboard input shape retained, implying that long wavelength features are well represented in our velocity models. The 2.5-degree input shows higher variability in resolution. The western part of CONUS, which has the densest GPS coverage, performs the best out of the entire study domain. Regions are less resolved where GPS coverage is low, particularly in the central part of CONUS encompassing Kansas, Nebraska, and the Dakotas.

We determine the optimal value of N for estimating the width of the Gaussian kernel by evaluating the trade-off between velocity model roughness and misfit for sequential values of N. For each value of N, we calculate roughness as the sum of a Laplacian operator convolved with the associated velocity field at every grid node. For misfit, we use the root-mean-square of the residual between GPS station velocities and the local value of the velocity model at each station location. The trade-off curve in Figure 3 shows misfit decreases as roughness increases. Choosing N at the maximum change in the trade-off curve as our optimal parameter (Figure 2 and S3), we construct our velocity field with $N = 20$.

Uncertainties in our GPS vertical velocity field originates from GPS station rate estimation and those propagated through the interpolation process. To come up with realistic uncertainties, we first compute the model misfit between our velocity field and the GPS station velocities. The model misfit serves as an appropriate baseline as a minimum uncertainty at the station locations. We then compute 95% confidence intervals of individual GPS time series rate estimate. Daily position uncertainties provided by data processing centers are dwarfed in comparison, hence negligible towards the final uncertainty estimates. We then put in the combined magnitude of model misfit and station rate uncertainties through our interpolation method exactly as we did for computing the

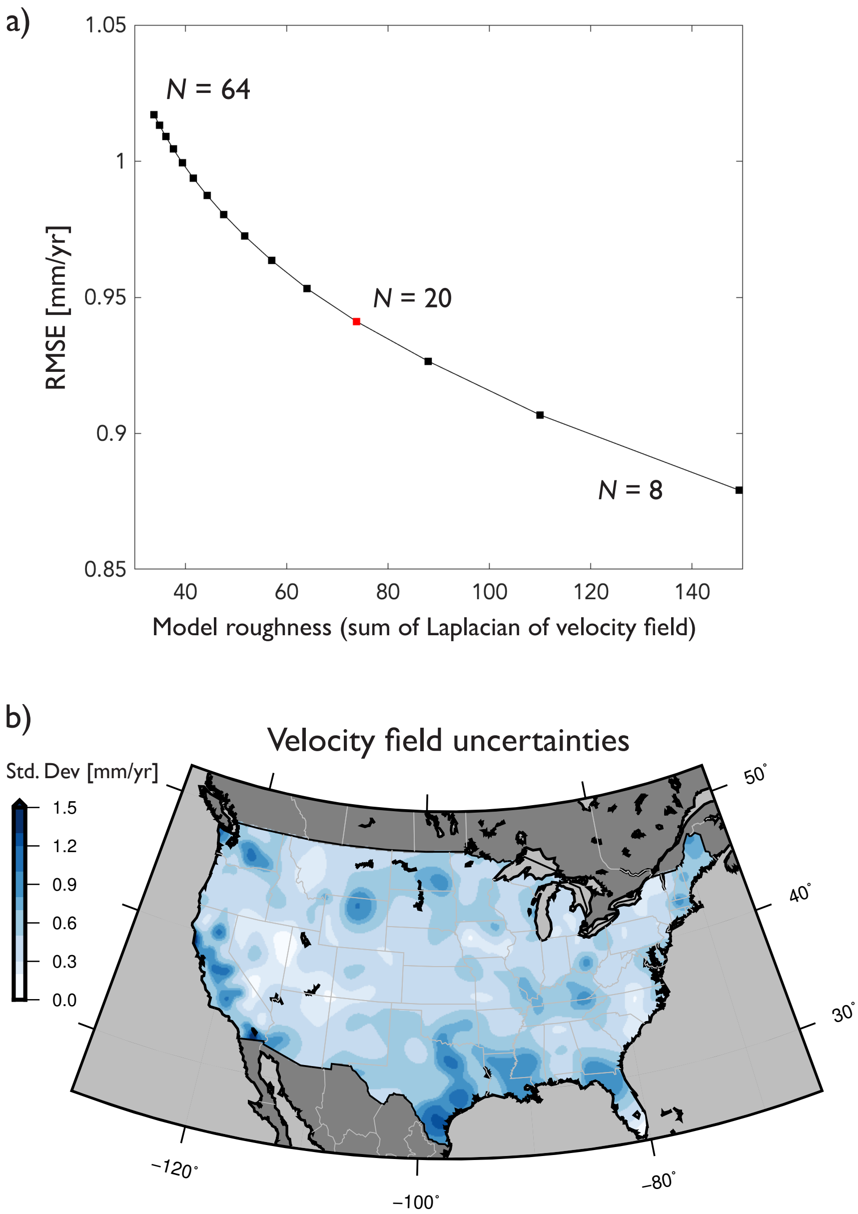

Figure 3. (a) Trade-off between velocity field roughness and root-mean-square misfit to GPS station velocities. The smoothness parameter N-centroids are plotted in increments of 4. The total root-mean-square of the GPS velocities is 1.74 mm/yr. Results using alternate selection of N are shown in Figures S4 and S5. (b) Uncertainty estimates of the GPS velocity field.

velocity fields, with the exception which arithmetic operations involving the input variables (uncertainties) follow the rules of error propagation. The resulting uncertainty field is illustrated in Figure 3.

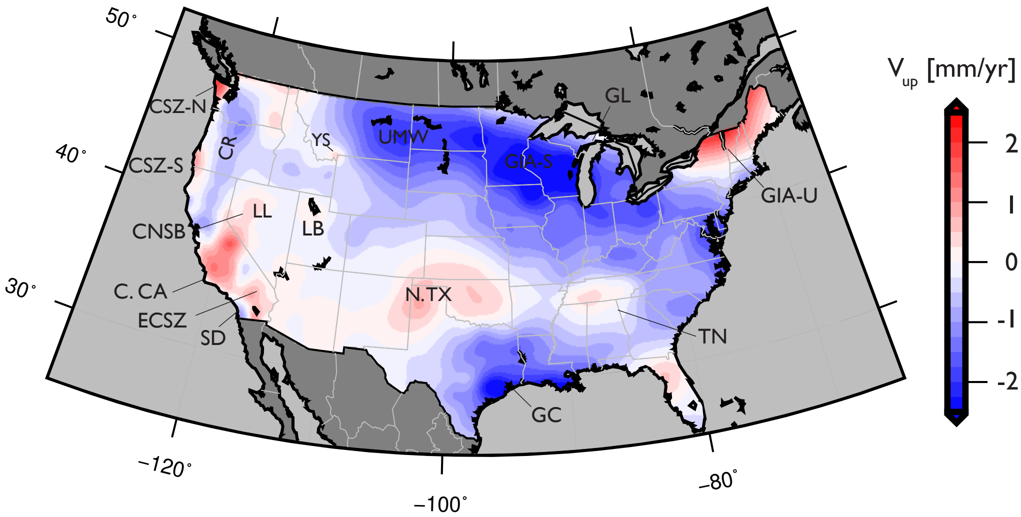

Figure 4. Vertical velocity field computed from 2007-2017 GPS time series. Major features that are discussed in the text are: C. CA (central California), CR (Cascade Range), CNSB (Central Nevada Seismic Belt), ECSZ (Eastern California Shear Zone), GIA-S (glacial isostatic adjustment subsidence), GIA-U (glacial isostatic adjustment uplift), GC (Gulf Coast), LB (Lake Bonneville), LL (Lake Lahonton), N. CSZ (northern Cascadia Subduction Zone), N. TX (northern Texas), S. CSZ (southern Cascadia Subduction Zone), SD (San Diego), TN (Tennessee), UMW (Upper Missouri River watershed), and YS (Yellowstone).

4 Results

The resulting vertical velocity field using $N = 20$ centroids is shown in Figure 4, with its associated uncertainties in Figure 3. All major features discussed below are labeled in the figure. We consider results within CONUS only, as only limited stations outside the boundary were used to constrain the velocity field. Within CONUS, the median and mean velocities are -0.50 mm/yr and -0.62 mm/yr respectively, with a variance from mean of 0.64 mm^2/yr^2. Root-mean-square residual between GPS station velocities and the local value of the velocity model at each station location is 0.94 mm/yr, although median misfit 0.46 mm/yr may be more useful, considering root-mean-square is more sensitive to outliers. The velocity field ranges from -2.83 mm/yr in Wisconsin just west of Lake Michigan to 2.21 mm/yr in the northern part of upstate New York, compared to -6.05 mm/yr to 6.87 mm/yr of the non-interpolated GPS station velocities. Features of various spatial scales presumably related to crustal tectonics, mantle dynamics, and surface mass loading are clearly observed and defined. However, localized deformation, such as individual fault motion, are likely to be attenuated or not visible due to the smoothing applied. The western United States (WUSA, west of the Rocky Mountains) exhibits more shorter wavelength vertical deformation than the eastern United States (EUSA) due to denser GPS distribution, and possibly reflecting the more localized tectonic environment formed by plate boundary deformation and crust-mantle interaction from the subducted Farallon plate (e.g. Forte et al., 2007; Liu & Stegman, 2011; Ghosh et al., 2013; Becker et al., 2015).

4.1 Vertical Deformation: Eastern United States

The dominant feature in EUSA is the near east-west trending subsidence belt across the northern Midwest due to glacial isostatic adjustment (GIA). The melting of the ice sheet induced an isostatic response from the mantle, leading to northward mantle flow and subsidence of the flexural bulge (Peltier & Andrews, 1976; Sella et al., 2007). Just northeast of the subsidence belt, GIA uplift can also be seen. However, not all the subsidence is caused by GIA, as a portion of it can be attributed to a recently observed increase in terrestrial water storage. For example, the sharp increase in water mass in the Great Lakes between 2013–2016 led to regional downward motion around the lakes due to elastic loading (Argus et al., 2019). Forward modeling the elastic Earth's response to the increased lake load yields a maximum subsidence rate of -0.94 mm/yr around the lake shore just west of Lake Michigan (Figure S6). Similarly, Lakes Fort Peck, Oahe, and Sakakawea in the Upper Missouri watershed saw large increase in lake levels over the ten years of our study period. These three lakes had a combined water volume increase that resulted in a maximum elastic subsidence rate of -0.41 mm/yr (Figure S7).

South of the subsidence forebulge are two broad regions of uplift, one bordering northern Texas and Oklahoma, and the other in Tennessee. Uplift in Texas and Oklahoma coincides with the southern portion of the High Plain aquifers. This region has been experiencing long-term groundwater loss from drought and agricultural extraction, which results in elastic uplift (Longuevergne et al., 2010). Since 1950, the southern High Plains have been steadily losing groundwater, with current groundwater volume estimated to be only 50% of its pre-agricultural development total (Haacker et al., 2016). Without sufficient recharge, this long-term depletion and associated uplift is projected to continue. The cause of uplift in Tennessee on the other hand, is less clear. No previous study has identified the cause of uplift, but climate and hydrology studies have shown that terrestrial water storage in the Ohio-Tennessee sub-water basin is particularly responsive to climate variability. Influenced by orographic effects of the Appalachian Mountains, this region exhibits a large hydrologic flux and seasonal variations in terrestrial water storage change (Seneviratne et al., 2004; Haacker et al., 2016), and a transient hydrologic unloading signature may be present in GPS observations. Interestingly, this region is also bounded by the Eastern Tennessee Seismic Zone and New Madrid Seismic Zone in the east and west (Powell et al., 1994; Tuttle et al., 2002), adding the possibility of the uplift being a tectonic feature.

Along the Gulf Coast, subsidence is known to be due to a combination of groundwater and hydrocarbon extraction in the Texas-Galveston area, accompanied by sediment compaction of the Louisiana Delta (Morton et al., 2006; Törnqvist et al., 2008; Dokka, 2011). The highest-amplitude subsidence in our velocity field occurs around Galveston and along the Louisiana coast, and we observe several smaller zones of subsidence inland. These zones correlate with major shale-gas production sites, which consume large amounts of groundwater for hydraulic fracturing (Nicot & Scanlon, 2012). The observed subsidence is likely to be caused by collapse of pore spaces in sediments from groundwater extraction (Chang et al., 2014). This implies that future monitoring of gas production can potentially be done by geodetic observations of ground subsidence.

4.2 Vertical Deformation: Western United States

In the WUSA, we are able to resolve complex deformation features of smaller scale ($\sim$50 km) with the variable-size interpolation kernel. Detailed features as localized as Yellowstone Caldera's uplift from magmatic and/or hydrothermal sources can be observed (Tizzani et al., 2015) in our velocity model. Along the Cascadia Subduction Zone, we observe elastic uplift due to the locking of the subduction interface in the northern and southern section, while the central section lacks similar motion, possibly due to partial fault creep (Dragert & Hyndman, 1995; McCaffrey et al., 2000; Schmalzle et al., 2014). One intriguing result from our velocity field is the prominent band of north-south subsidence 250-300 km east of the Cascadia trench, spanning Washington to northern California. A possible explanation for this subsidence is elastic loading from increased terrestrial water storage in the Cascade Ranges. Fu et al. (2015) shows that precipitation in the Pacific Northwest is localized in high altitude areas along the Cascade Ranges, coincident with observed subsidence. The subsidence does, however, extend south beyond the Cascades. An alternate explanation is of interseismic subsidence from mantle flow associated with the Cascadia megathrust (Hashima & Sato, 2017; Johnson & Tebo, 2018; Yousefi et al., 2020). Some of these models predict interseismic inland subsidence to be monotonic but accelerating over decadal timescales. Further investigation of the temporal evolution of this subsidence feature will benefit both subduction zone and terrestrial water storage studies.

Much of central California exhibits uplift. Recent studies have examined hydrology-driven elastic uplift (Borsa et al., 2014; Amos et al., 2014), mountain building processes of the Sierra Nevada (Hammond et al., 2016), and recent inflation episodes of the Long Valley Caldera (Montgomery-Brown et al., 2015; Hammond et al., 2019; Silverii et al., 2020). Since these processes happen concurrently, it is difficult to partition the observed velocities into individual components. Time series, however, might provide important constraints as these processes operate at different time scales. Deformation due to localized tectonic activities, such as low magnitude earthquakes, may not be consistent features over a decade or longer, unlike longer topography building processes. One would also expect smoother spatial footprint from hydrologic loading (Farrell, 1972), compared to localized tectonic activities along faults or volcanoes. We note that there is on-going large amplitude subsidence within the Central Valley driven by poroelastic processes from agricultural groundwater withdrawal. Such deformation is well documented in other geodetic studies (Hammond et al., 2016; Neely et al., 2020), but since only the elastic effect of land hydrology is examined in this study, GPS stations within the Central Valley are excluded (see Figure S8 for a version of the velocity field including stations heavily affected by poroelastic effects).

Vertical deformation in Southern California primarily appears to represent different stages of the earthquake cycle. The footprint of post-seismic deformation from the Hector Mine, Landers, and El Mayor-Cucapah earthquakes can be observed in the uplift at the Eastern California Shear Zone and the Salton Trough, which is caused by the relaxation of mantle coupled with the lower crust (Pollitz et al., 2001; Freed et al., 2007; Rollins et al., 2015). The observed subsidence near San Diego may due to the interplay between these post-seismic transients and the change in rheology west of the Peninsular Range (Rollins et al., 2015). Bending moments from the locked portion of the San Andreas Fault could also be responsible for this subsidence (Smith-Konter et al., 2014).

Finally, two uplift regions are observed in the Basin and Range Province, driven by viscoelastic deformation from two different processes. The first one is the viscoelastic response to the drying up of Lakes Bonneville and Lahonton. Shoreline studies and modeling show that the lake basins have accumulated 22 m of uplift in the past 13,000 years, and are uplifting currently at a rate of 1.7 mm/yr at Lahonton and 0.1 mm/yr at Bonneville (Adams et al., 1999; Nakiboglu & Lambeck, 1983). The second process is post-seismic deformation from the 1915–1954 Central Nevada Seismic Belt earthquake sequence. Viscoelastic relaxation of $2-3$ mm/yr from two normal fault earthquakes ($M_w 7.3, 6.8$) were observed using Interferometric Synthetic Aperture Radar (Gourmelen & Amelung, 2005). Separating lake rebound uplift from post-seismic signal will be particularly useful in providing additional constraints for upper mantle viscosity and shape of Laurentide ice sheet in the WUSA, as demonstrated recently by Austermann et al. (2020) for example.

4.3 GIA, hydrological loading, and translation motion of Earth's center of mass

The three GIA models considered here (IEC5G, ICE-6G_D, and Caron et al.) all over-predict subsidence south of the former ice sheet forebulge, producing long wavelength residual uplift across CONUS (Figure 5). The forebulge subsidence in our velocity model is best modeled by ICE-6G_D, albeit with residual subsidence near Minnesota (-98^o E/48^o N); the other two models leave residual signal that is larger in amplitude and spatial scale. We certainly do not expect a perfect fit from these GIA models, especially since lateral mantle viscosity variation is typically not considered in global GIA models. The sharp change in residual velocities near the forebulge suggests that lateral viscosity variations may have to be considered to account for localized GIA response (e.g. Latychev et al., 2005; Li et al., 2020). Compared to the original velocity field's variance of 0.64 mm^2/yr^2, the variances of the residual fields after correction are: ICE-5G = 1.08 mm^2/yr^2, ICE-6G_D = 0.51 mm^2/yr^2, Caron = 1.13 mm^2/yr^2. These numbers suggest ICE-6G_D is the most representative model of current GIA motion as observed by GPS. However, ICE-6G_D is in fact more heavily constrained by GPS data compared to other models that also include geodetic constraints (e.g. ICE-5G), hence having the largest variance reduction does not come as a surprise. Uncertainties of global GIA models are generally not well defined, and issues arise, for example, due to inter-related rheological and ice sheet uncertainties. Methods of uncertainty estimations range from presumed confidence interval to Bayesian inference (e.g. Paulson et al., 2007; Caron et al., 2018), but recent evaluation of uncertainty across a suite of GIA models suggest far field uncertainty in North America is approximately $0.3 - 0.5$ mm/yr (Simon & Riva, 2020), which most of the residuals here exceed.

We compute vertical deformation rates due to the elastic Earth's response to hydrologic loading using terrestrial water storage (TWS) estimates from GRACE (Figure 6). Deformation due to hydrologic loading has a mean rate of 0.03 mm/yr over CONUS. It ranges from -0.68 mm/yr to 1.04 mm/yr, encompassing two major uplift regions (central California, northern Texas) and three subsidence regions (the Great Lakes, the Upper Missouri watershed, and the South Atlantic-Gulf watershed). Qualitatively, GRACE-derived mass loads match up with major deformation features visible in our GPS velocity field. These regions are all known to exhibit long-term change in TWS as a result of

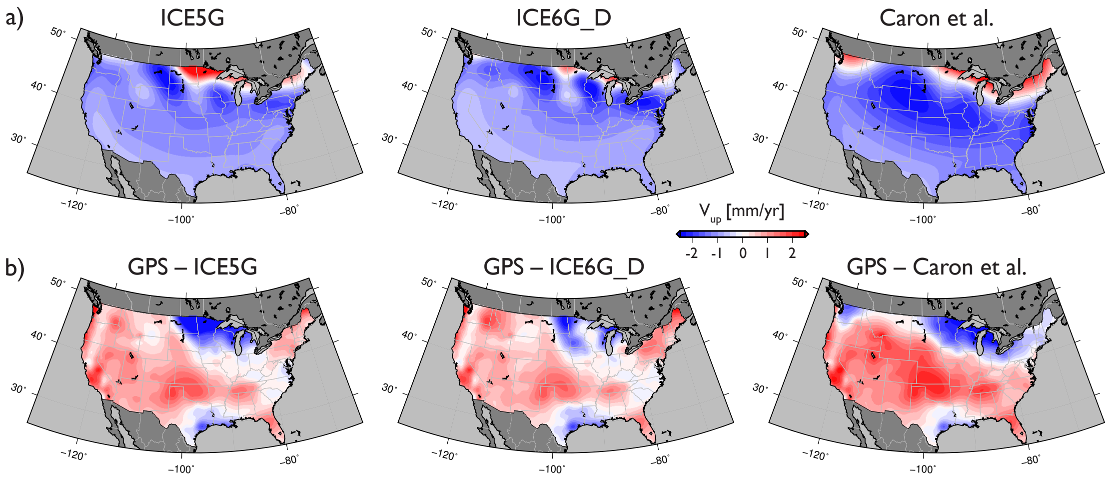

Figure 5. a) Vertical rates predicted by ICE-5G (VM2), ICE-6G_D (VM5a), and Caron et al. (b) Residual velocities after removing model predictions from GPS velocity field.

climate variability as well as human impact (Rodell et al., 2018; Adusumilli et al., 2019). For the subsidence regions in the Great Lakes and Upper Missouri watershed, GRACE sees not only the increased lake water mass as mentioned above (Lakes Fort Peck, Oahe, Sakakawea, Figure S6 and S7), but also the overall increased water storage in the surrounding watersheds.

Given the $\sim$ 300 km spatial resolution of GRACE TWS's estimates, simply removing GRACE-derived elastic deformation from the GPS field leaves residual short wavelength features that cannot be resolved by satellite gravity measurements. We therefore apply a 300 km (2σ) Gaussian filter to our GPS velocity field in order to facilitate comparison between the two fields; this product will now be referred as the "smoothed field", and the original velocity field as "unsmoothed". Figure 6 shows the residuals obtained after removing GRACE-derived hydrology loading from the unsmoothed GPS velocity field, as well as the residuals from using the smoothed GPS velocity field. The two uplift regions in California and Texas are reduced to nearly zero in the hydrology-corrected smoothed GPS velocity field. This suggests that the hydrologic loading is a key component of observed vertical velocities and that a full-resolution TWS estimate would explain even more of the variance in our GPS velocity field.

Table 1 shows the mean and variance of the velocity field with different components taken out. In both the unsmoothed and smoothed GPS velocity field cases, we see substantial variance reduction from simply removing the ICE-6G_D GIA model prediction and GRACE-derived hydrologic loading estimates. Removing GIA reduces variance by

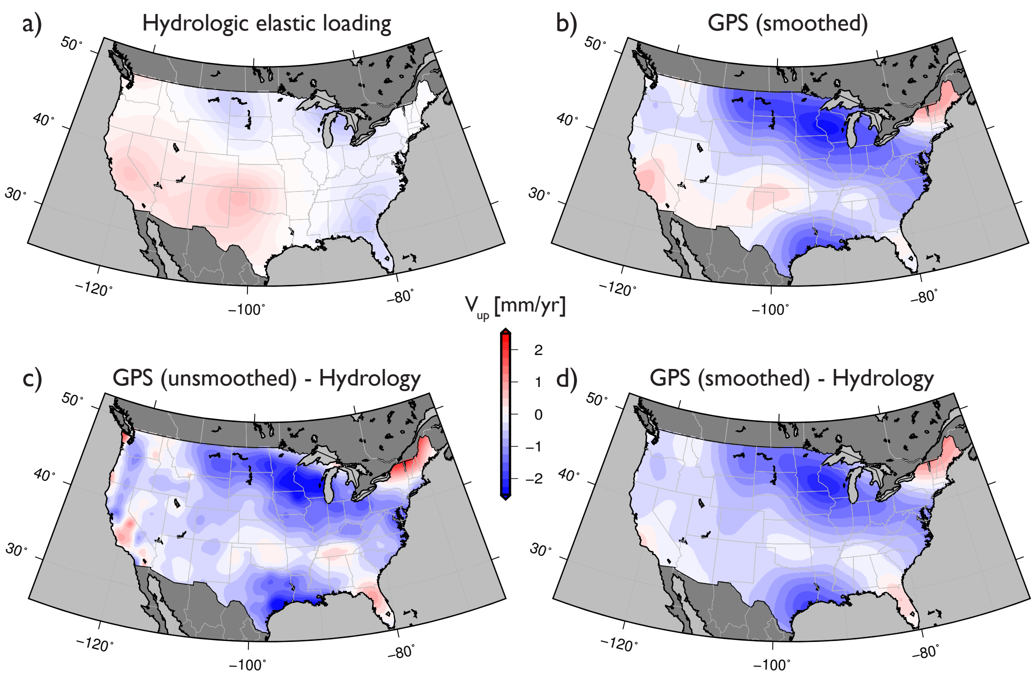

Figure 6. (a) Vertical rates due to elastic hydrologic loading, modeled using CSR GRACE-derived terrestrial water storage estimates as input load. (b) 300 km Gaussian smoothed GPS velocity field. (c) Residual velocities after removing hydrologic loading rates from GPS velocity field. (d) Residual velocities after removing hydrologic loading rates from the 300 km Gaussian smoothed GPS velocity field.

20%, removing hydrologic loading reduces variance by 28%, and removing both components reduces variance by 36%. The removal of GRACE from the smoothed field reduces a higher percentage of velocity variability than in the unsmoothed field, which is indicative of GPS and GRACE matching up well at 300 km resolution and less so at shorter scales. The GIA correction, on the other hand, performs worse in the smoothed field, as the details captured by GPS are smeared out. These statistics therefore indicate that GIA and GRACE TWS corrections are valid when applied to velocity data at appropriate wavelengths. However, removing GIA and hydrologic loading components also leads to broad residual uplift across CONUS (Figure 7), as evident in the residual mean of 0.40 mm/yr. While mantle dynamics can produce long wavelength deformation, a tectonic origin for such feature is unlikely, as recent mantle tomography models have shown thermal anomalies under North America at smaller scale (Schmandt & Lin, 2014; Schaeffer & Lebedev, 2014). One plausible explanation is related to bias in geocenter origin. GPS measurements are referenced to Earth's center of mass (CM) in ITRF2008 (Altamimi et al., 2011), and the translation motion of CM (also known as geocenter motion) may appear in GPS measurements as a deformation signal. Following Argus, Peltier, et al. (2014) and Argus et al. (2017), we evaluate vertical velocities on our velocity grids due to the translation velocity of Earth's center of mass of $X = 0.18$ mm/yr, $Y = -0.13$ mm/yr, and $Z = 0.56$ mm/yr. This translation motion explains most of the apparent uplift in CONUS (Figure 7). Removing CM translation leaves a mean residual velocity of -0.032 mm/yr. CM translation has little effects on relative uplift and subsidence between shorter wavelength features, as it simply acts as a near constant ramp across the continent; both the smoothed and unsmoothed variance remain unchanged after its removal. A recent study by Ding et al. (2019) arrives at a similar conclusion, when geocenter motion correction is applied to GPS data along the East Coast. The resulting velocities, combined with tide gauge data, lead to East Coast sea level rise estimates closer to the global mean rate. Together with results presented in this study, the improved fit to independent sets of velocity data by correcting for geocenter motion suggests such motion is important in interpreting long wavelength geodetic observations.

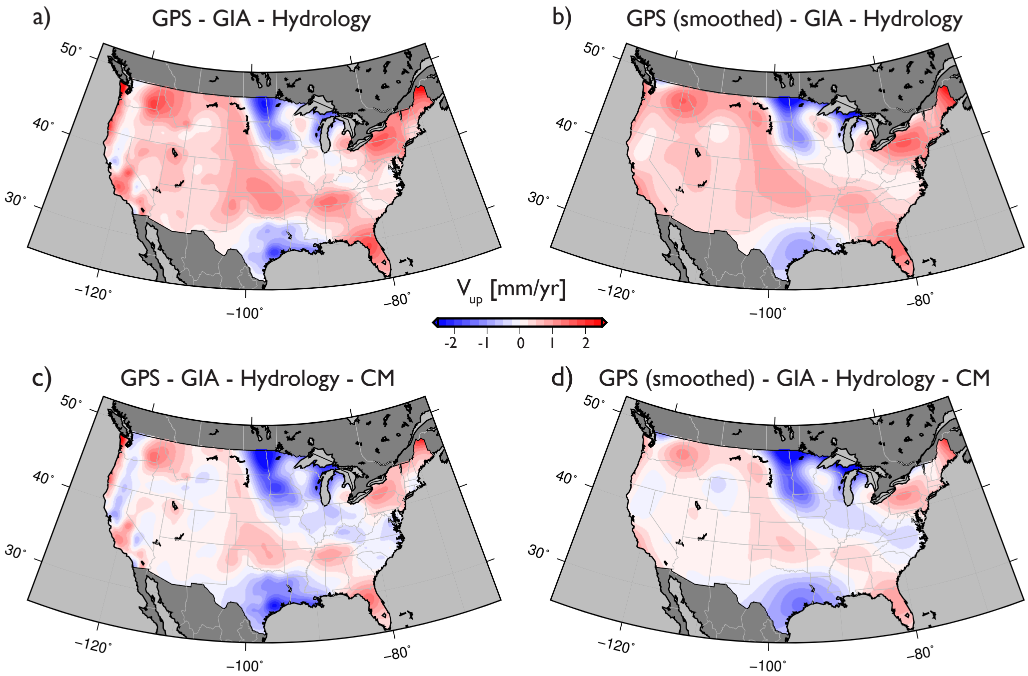

Figure 7. (a, d) Residual field after removing, GIA, hydrologic loading, and center of mass translation (CM) from unsmoothed GPS velocity field. (b, c). Same as left, but with smoothed GPS velocity field. Additional intermediate steps can be found in Figure S9.

Table 1. Mean velocities and variances of the original GPS velocity field and residual velocity fields after removing GIA (ICE-6G_D), hydrology, and center of mas translation (CM). Variance percentage changes compared to the GPS velocity field are in parentheses. Right-most column shows the variances using an initially smoothed out (300-km Gaussian) GPS velocity field. Variance of residual fields decreases as each component is taken out.

	Mean	Variance, unsmoothed	Variance, smoothed
GPS	−0.62 mm/yr	0.64 mm^2/yr^2	0.49 mm^2/yr^2
GPS - GIA	0.42 mm/yr	0.51 mm^2/yr^2 (−20%)	0.45 mm^2/yr^2 (−8.1%)
GPS - hydrology	−0.64 mm/yr	0.46 mm^2/yr^2 (−28%)	0.31 mm^2/yr^2 (−37%)
GPS - hydrology - GIA	0.40 mm/yr	0.41 mm^2/yr^2 (−36%)	0.35 mm^2/yr^2 (−28%)
GPS - hydrology - GIA - CM	−0.032 mm/yr	0.41 mm^2/yr^2 (−36%)	0.35 mm^2/yr^2 (−28%)

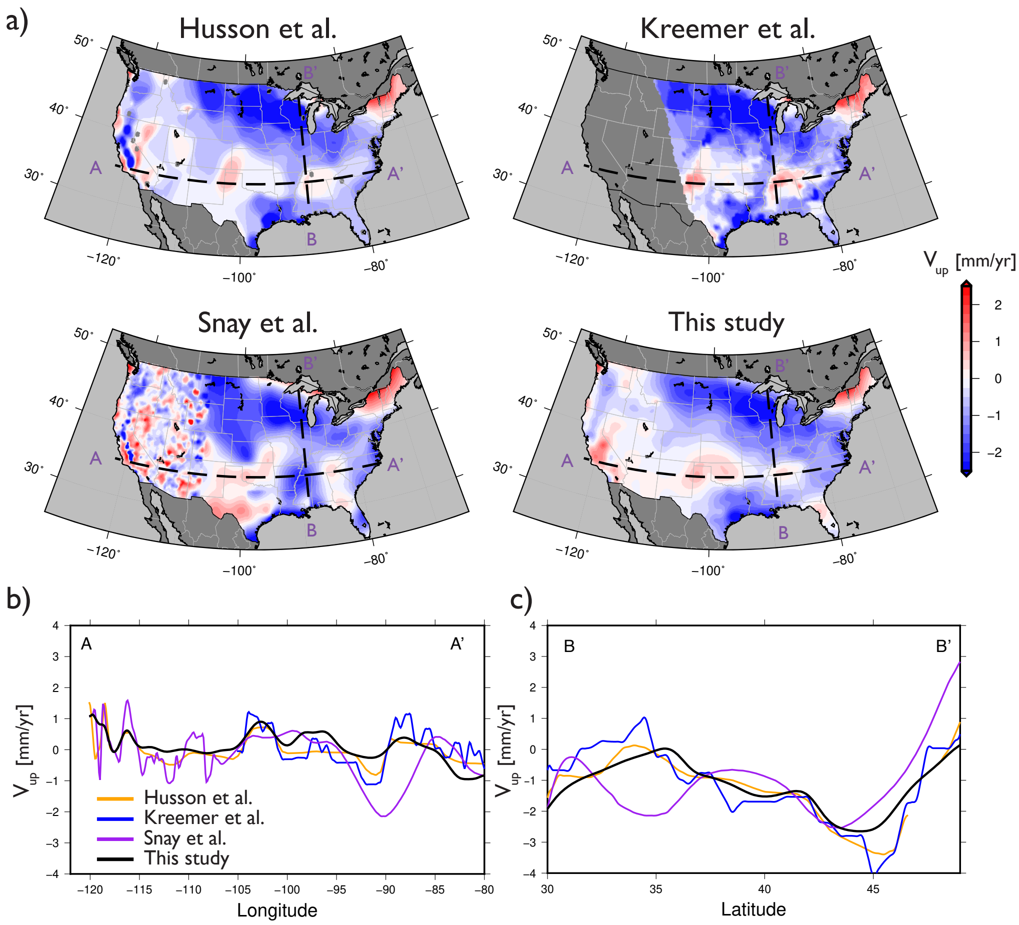

Figure 8. (a) Comparison of velocity fields by Husson et al. (2018), Kreemer et al. (2018), Snay et al. (2016), and this study. (b,c) Longitudinal and latitudinal profiles from the above fields; Husson et al. (orange), Kreemer et al. (blue), Snay et al. (purple), this study (black).

4.4 Comparison with published velocities

We compare our results with three other continental scale CONUS vertical velocities in Figure 8: from Snay et al. (2016), Husson et al. (2018), and Kreemer et al. (2018). Note that Snay et al.'s results are combined with the updated WUSA results shown in Snay et al. (2018). Our velocity field most resembles Husson et al.'s, with a mean difference of -0.15 mm/yr and variance of the difference being 0.24 mm^2/yr^2. Table 2 shows the mean and variance of differences between all four velocity fields, considering only the common grid points. Visually, long wavelength features look generally similar, and indeed, by applying 300 km Gaussian filters to all four velocity fields, large scale GIA subsidence at the former ice sheet forebulge, Gulf Coast, and uplift in California, Texas are observed (Figure S10).

In contrast, noticeable differences can be seen in shorter wavelength details. To provide a clearer picture of these differences, we extract two profiles of the four velocity fields, a longitudinal one at 35^oN, and a latitudinal one at 90^oE (dashed line in Figure 8a). Both profiles show short wavelength deviations between the four velocity fields. In profile A-A', the transition from relative uplift to subsidence between -95^oE and -85^oE is sharpest in Kreemer et al.'s velocity field. In Profile B-B', GIA's forebulge subsidence north of 40^oN is similar among all four fields. Discrepancies are larger at the southern portion of the profile, where smaller scale features south of Tennessee differ by up to ~ 3 mm/yr. These differences are in part a reflection of the methods used in constructing the velocity fields in each of the studies. The use of Voronoi tessellation in Husson et al. leads to sharper gradients, while our incorporation of Gaussian weighting leads to smoother transitions between features than Delauney triangulation in Kreemer et al. While the differences in computing GPS station rates, i.e. MIDAS (Blewitt et al., 2016) vs. linear least squares fitting, do not lead to significant disagreements in long wavelength features, regions where GPS coverage is low or stations with highly non-linear signal may be more affected. It is therefore important to use information from multiple GPS stations to interpolate a grid node, and for future studies to consider the potential effects of choosing a particular data processing method.

It is difficult to provide a quantitative comparison of these results for several reasons. First, the spatial coverages of CONUS in these studies are different. Kreemer et al. studied deformation east of the Rocky Mountains, while Snay et al. divided their velocity computations into eastern and western regions with a change in resolution near -107^oE. Secondly, GPS temporal coverage varies between these studies. For example, Kreemer et al. used time series as short as 1.5 years, while we specified time series that are at least 6 years long within our 2007–2017 study period. This may contribute to the short wavelength variability between the four velocity fields, as shorter time series may reflect transient process and increased noise level. However, long wavelength deformation in all four solutions is similar, suggesting those features are not temporary. We cannot be certain they are all caused by secular geological processes either, as GPS measurements only date back $\sim$20 years. Thirdly, we choose to omit GPS stations that are strongly affected by poroelastic effects from groundwater in California's Central Valley, since including these stations would affect our interpretation of hydrology-related elastic deformation. We therefore cannot directly compare our California velocities with those from Snay et al. and Husson et al., which included those stations.

Table 2. (Upper triangle) Variance of the differences between four velocity fields. (Lower triangle) Mean of the differences between four velocity fields. Only grid points that are common in all four fields are considered.

	This study	Kreemer et al.	Husson et al.	Snay et al.
This study		0.37 mm^2/yr^2	0.20 mm^2/yr^2	0.59 mm^2/yr^2
Kreemer et al.	0.16 mm/yr		0.16 mm^2/yr^2	0.79 mm^2/yr^2
Husson et al.	0.15 mm/yr	0.07 mm/yr		0.68 mm^2/yr^2
Snay et al.	0.04 mm/yr	0.22 mm/yr	0.319 mm/yr	

5 Discussion

Studies of continental-scale vertical deformation within CONUS have traditionally focused on the impact of glacial isostatic adjustment. In this work we show that careful analysis of GPS station motion reveals spatially coherent vertical deformation features beyond the signature of GIA. We attempt to remove known vertical deformation from GIA and hydrologic loading from the GPS-derived velocity field to see if known processes can explain the observed velocity field. These adjustments result in a total reduction in variance of 36% and a residual velocity that is our best estimate of long-term motion from tectonics, non-GIA isostasy, and potentially mantle dynamics.

Given the relatively short time span of GPS observations, some of what appears to be secular motion actually could be transient processes operating at decadal to century time scales. One well known source of transient process is hydrologic loading, whose broad-scale decadal signature we addressed in this study. Hydrologic loading is driven by climate variability; for example, changes in California's TWS in the past decade range from multiyear drought caused by El Nino Southern Oscillation events (Seager et al., 2015) to rapidly increased precipitation from week-long atmospheric rivers (Adusumilli et al., 2019). On the tectonics side, there are transient features that span interannual to century time scales. Viscoelastic deformation from older earthquakes may appear nearly linear in GPS time series e.g. Hearn et al. (2013), but post-seismic deformation from recent earthquakes, such as the 2010 El-Mayor Cucapah event, may still manifest as exponential decay transients. Non-linear episodic inflation in Long Valley and Yellowstone Calderas are governed by intrusion of magmatic materials and movement of volatiles (Hurwitz & Lowenstern, 2014). Some of the transient features discussed in this study are located along the coast, potentially affecting long-term relative sea level estimates. This is particularly true for the West Coast, which exhibits higher vertical land motion variability than the East Coast and the Gulf of Mexico; vertical uplift rates there at times are comparable with the regional mean sea level rise (National Research Council, 2012), hence improved vertical land motion estimates are needed to better understand threats from the rising sea. Our velocity field is therefore a snapshot of the current state of deformation; understanding the underlying drivers of secular vertical deformation requires removing transient processes from the observations.

To achieve this goal will require overcoming several challenges in modeling GIA and hydrological loading. A potential source of GIA mismodeling is from the increasing use of GPS data to constrain present-day motion in GIA models. The constructions of recent GIA models incorporate more GPS data than ever (Peltier et al., 2018; Caron et al., 2018). GPS data improve the accuracy of these models, however, as discussed above, there are other processes that contribute to vertical motion in GPS data. One example is the water volume fluctuations in the Great Lakes, which produce observable deformation in GPS around the GIA subsidence region. Incorporating GPS stations affected by this non-GIA related deformation into models can lead to mismodeling of the actual forebulge collapse subsidence. When looking at highly rebounding areas such as the former ice domes (regions where the last remnants of the ice sheets melted in high latitude areas), the misfit-to-amplitude ratios are low and mostly negligible. For CONUS, where vertical rates are within ~ 3 mm/yr, the same misfit level would result in incorrect interpretation of crustal motion.

In section 4.3, we show that displacements from GRACE TWS-derived estimates of hydrology loading successfully remove some major elastic uplift features in a smoothed version of our velocity field. There are merits to having both the rougher and smoother fields. Looking at the smoothed version, GPS velocities are indeed capturing the overall elastic loading signal from hydrology, suggesting at long-wavelength spatial scale GRACE can help constraint such process. However, interpretation of the smoothed velocity field is limited to long wavelength features. Detailed features, particularly near the plate boundary in the west are lost in the smoothing process. On the other hand, removing GRACE-derived loading rates from the rougher version does not fully remove elastic loading at shorter spatial scales. Figure S11 shows the spatial velocity gradients prior and after removing GRACE-derived TWS estimates. High gradients can be seen in regions that experience high TWS variability, such as California and the Great Lakes. While applying GRACE-derived TWS correction reduces the amplitude of GPS vertical rates as seen in Figure 6, some short-wavelength gradients remain. This highlights the need to downscale TWS estimates in future work, as there are short-scale hydrological loading features that are not well-modeled using low-resolution GRACE alone. Recent studies have either used GPS, GRACE, and hydrologic model individually (Argus, Fu, & Landerer, 2014; Fu et al., 2015; Tregoning et al., 2009; Argus et al., 2017) or combined them to invert for seasonal to interannual TWS anomalies (Adusumilli et al., 2019). With GRACE as a volumetric constraint and GPS/hydrologic models as spatial constraint, expanding such analysis to continental scale can improve the spatial resolution of the hydrologic load displacement model, whose removal will yield a higher resolution hydrologic loading-free vertical field for future studies of solid earth processes.

6 Conclusion

A robust vertical crustal velocity field for the contiguous United States is computed from 2007–2017 pointwise velocity estimates at 2782 GPS stations in the region. We are able to extract deformation patterns at variable resolution using an adaptive interpolation method, and identify deformation due to GIA, lithospheric tectonics, elastic deformation from hydrologic loading, and anthropogenic activities. In the west, we image the clear signatures of short wavelength subduction zone tectonics and dynamics, magmatic activity, and post-seismic deformation. In the east, a majority of the deformation is related to GIA and hydrologic activities. Comparing our results to three other studies, we observe that while long wavelength signals are similar in amplitude and spatial pattern in all four velocity fields, there are substantial differences in shorter scale features that mainly arise from different temporal coverage of raw data and data processing methods.

By removing deformation predicted by GIA models and elastic loading from GRACE TWS, we are able to reduce the variance of the velocity field by 36%. We demonstrate that hydrologic loading can be partially corrected by GRACE TWS estimates at ~ 300 km wavelength, but it lacks the resolution to resolve shorter-wavelength, high gradient features caused by localized surface loads. Correcting for Earth's center of mass translation motion, as proposed by Argus, Peltier, et al. (2014), reduces the mean velocity of the residuals from -0.40 mm/yr to -0.032 mm/yr, which suggests this motion does affect observed GPS vertical rates and that future studies should correct for. Future work on downscaling continental-scale hydrologic loading will help partition hydrology-induced motion more accurately, bringing us closer to understanding non-GIA secular vertical deformation.

Acknowledgments

This study is funded by NASA grant NNX16AL97G; work conducted at Scripps Institution of Oceanography is partially supported by Folsom Graduate Fellowship. GPS daily position data processed by the Nevada Geodetic Laboratory can be found at

http://geodesy.unr.edu/NGLStationPages/GlobalStationList (Blewitt et al., 2018),

last accessed August 2, 2019. Individuals and operators who contribute to raw RINEX data are documented under each station. We thank editor Paul Tregoning, and reviewers Jeffrey Freymueller and Laurent Husson for their thoughtful comments and reviews. We also thank Corne Kreemer, Laurent Husson, and Richard Snay for providing their velocity fields, and Deborah Kilb and Stephanie Mumma for compiling lake loading displacements. Discussions with Susheel Adusumilli, Wesley Neely, and Christopher Johnson are well appreciated. Dataset generated from this research is available at

https:doi.org/10.5281/zenodo.3963343.

References

Adams, K. D., Wesnousky, S. G., & Bills, B. G. (1999). Isostatic rebound, active faulting, and potential geomorphic effects in the Lake Lahontan basin, Nevada and California. *GSA Bulletin*, *111*(12), 1739–1756. doi: 10.1130/0016-7606(1999)111⟨1739:IRAFAP⟩2.3.CO;2

Adusumilli, S., Borsa, A. A., Fish, M. A., McMillan, H. K., & Silverii, F. (2019). A Decade of Water Storage Changes Across the Contiguous United States From GPS and Satellite Gravity. *Geophysical Research Letters*, *46*(22), 13006–13015. doi: 10.1029/2019GL085370

Agnew, D. C. (1997). NLOADF: A program for computing ocean-tide loading. *Journal of Geophysical Research: Solid Earth*, *102*(B3), 5109–5110. doi: 10.1029/96JB03458

Altamimi, Z., Collilieux, X., & Métivier, L. (2011). ITRF2008: an improved solution of the international terrestrial reference frame. *Journal of Geodesy*, *85*(8), 457–473. doi: 10.1007/s00190-011-0444-4

Amos, C. B., Audet, P., Hammond, W. C., Bürgmann, R., Johanson, I. A., & Blewitt, G. (2014). Uplift and seismicity driven by groundwater depletion in central California. *Nature*, *509*(7501), 483–486. doi: 10.1038/nature13275

Argus, D. F., Fu, Y., & Landerer, F. W. (2014). Seasonal variation in total water storage in California inferred from GPS observations of vertical land motion. *Geophysical Research Letters*, *41*(6), 1971–1980. doi: 10.1002/2014GL059570

Argus, D. F., Landerer, F. W., Wiese, D. N., Martens, H. R., Fu, Y., Famiglietti, J. S., ... Watkins, M. M. (2017). Sustained Water Loss in California's Mountain Ranges During Severe Drought From 2012 to 2015 Inferred From GPS. *Journal of Geophysical Research: Solid Earth*, *122*(12), 10,559–10,585. doi: 10.1002/2017JB014424

Argus, D. F., Peltier, W. R., Drummond, R., & Moore, A. W. (2014). The Antarctica component of postglacial rebound model ICE-6G_c (VM5a) based on GPS positioning, exposure age dating of ice thicknesses, and relative sea level histories. *Geophysical Journal International*, *198*(1), 537–563. (Publisher: Oxford Academic) doi: 10.1093/gji/ggu140

Argus, D. F., Ratliff, B., DeMets, C., Borsa, A. A., Wiese, D. N., Kreemer, C., ... Crowley, J. W. (2019). Sinking of the Upper Midwest, rise of the Great Lakes, and collapse of the Laurentide Ice Sheet forebulge. AGU.

Austermann, J., Chen, C. Y., Lau, H. C. P., Maloof, A. C., & Latychev, K. (2020, February). Constraints on mantle viscosity and Laurentide ice sheet evolution from pluvial paleolake shorelines in the western United States. *Earth and Planetary Science Letters*, *532*, 116006. doi: 10.1016/j.epsl.2019.116006

Becker, T. W., Hardebeck, J. L., & Anderson, G. (2005). Constraints on fault slip rates of the southern California plate boundary from GPS velocity and stress inversions. *Geophysical Journal International*, *160*(2), 634–650. (Publisher: Oxford Academic) doi: 10.1111/j.1365-246X.2004.02528.x

Becker, T. W., Lowry, A. R., Faccenna, C., Schmandt, B., Borsa, A., & Yu, C. (2015). Western US intermountain seismicity caused by changes in upper mantle flow. *Nature*, *524*(7566), 458–461. doi: 10.1038/nature14867

Bennett, R. A., Wernicke, B. P., Niemi, N. A., Friedrich, A. M., & Davis, J. L. (2003). Contemporary strain rates in the northern Basin and Range province from GPS data. *Tectonics*, *22*(2). doi: 10.1029/2001TC001355

Blewitt, G., Hammond, W. C., & Kreemer, C. (2018). Harnessing the GPS Data Explosion for Interdisciplinary Science. *Eos*, *99*. doi: 10.1029/2018EO104623

Blewitt, G., Kreemer, C., Hammond, W. C., & Gazeaux, J. (2016). MIDAS robust trend estimator for accurate GPS station velocities without step detection. *Journal of Geophysical Research: Solid Earth*, *121*(3), 2054–2068. doi: 10.1002/2015JB012552

Blewitt, G., & Lavallée, D. (2002). Effect of annual signals on geodetic velocity. *Journal of Geophysical Research: Solid Earth*, *107*(B7), ETG 9–1–ETG 9–11. doi: 10.1029/2001JB000570

Bock, Y., & Melgar, D. (2016). Physical applications of GPS geodesy: a review. *Reports on Progress in Physics*, *79*(10), 106801. doi: 10.1088/0034-4885/79/10/106801

Borsa, A. A., Agnew, D. C., & Cayan, D. R. (2014). Ongoing drought-induced uplift in the western United States. *Science*, *345*(6204), 1587–1590. doi: 10.1126/science.1260279

Calais, E., Han, J. Y., DeMets, C., & Nocquet, J. M. (2006). Deformation of the North American plate interior from a decade of continuous GPS measurements. *Journal of Geophysical Research: Solid Earth*, *111*(B6). doi: 10.1029/2005JB004253

Caron, L., Ivins, E. R., Larour, E., Adhikari, S., Nilsson, J., & Blewitt, G. (2018). GIA Model Statistics for GRACE Hydrology, Cryosphere, and Ocean Science. *Geophysical Research Letters*, *45*(5), 2203–2212. doi: 10.1002/2017GL076644

Chang, C., Mallman, E., & Zoback, M. (2014). Time-dependent subsidence associated with drainage-induced compaction in Gulf of Mexico shales bounding a severely depleted gas reservoirTime-dependent Subsidence Associated with Shale Compaction. *AAPG Bulletin*, *98*(6), 1145–1159. (Publisher: GeoScienceWorld) doi: 10.1306/11111313009

Cleveland, R., Cleveland, W., McRae, J., & Terpenning, I. (1990). STL: A seasonal-trend decomposition procedure based on loess. *Journal of Official Statistics*, *6*(1), 3–33.

Davis, J. L., & Mitrovica, J. X. (1996). Glacial isostatic adjustment and the anomalous tide gauge record of eastern North America. *Nature*, *379*(6563), 331–333. doi: 10.1038/379331a0

Ding, K., Freymueller, J. T., He, P., Wang, Q., & Xu, C. (2019). Glacial Isostatic Adjustment, Intraplate Strain, and Relative Sea Level Changes in the Eastern United States. *Journal of Geophysical Research: Solid Earth*, *124*(6), 6056–6071. doi: 10.1029/2018JB017060

Dokka, R. K. (2011). The role of deep processes in late 20th century subsidence of New Orleans and coastal areas of southern Louisiana and Mississippi. *Journal of Geophysical Research: Solid Earth*, *116*(B6). doi: 10.1029/2010JB008008

Dragert, H., & Hyndman, R. D. (1995). Continuous GPS monitoring of elastic strain in the Northern Cascadia Subduction Zone. *Geophysical Research Letters*, *22*(7), 755–758. doi: 10.1029/95GL00469

Farrell, W. E. (1972). Deformation of the Earth by surface loads. *Reviews of Geophysics*, *10*(3), 761–797. doi: 10.1029/RG010i003p00761

Fialko, Y. (2004). Evidence of fluid-filled upper crust from observations of postseismic deformation due to the 1992 Mw7.3 Landers earthquake. *Journal of Geophysical Research: Solid Earth*, *109*(B8). doi: 10.1029/2004JB002985

Forte, A. M., Mitrovica, J. X., Moucha, R., Simmons, N. A., & Grand, S. P. (2007).

Descent of the ancient Farallon slab drives localized mantle flow below the New Madrid seismic zone. *Geophysical Research Letters*, *34*(4). doi: 10.1029/2006GL027895

Freed, A. M., Ali, S. T., & Bürgmann, R. (2007). Evolution of stress in Southern California for the past 200 years from coseismic, postseismic and interseismic stress changes. *Geophysical Journal International*, *169*(3), 1164–1179. (Publisher: Oxford Academic) doi: 10.1111/j.1365-246X.2007.03391.x

Fu, Y., Argus, D. F., & Landerer, F. W. (2015). GPS as an independent measurement to estimate terrestrial water storage variations in Washington and Oregon. *Journal of Geophysical Research: Solid Earth*, *120*(1), 552–566. doi: 10.1002/2014JB011415

Gazeaux, J., Williams, S., King, M., Bos, M., Dach, R., Deo, M., ... Webb, F. H. (2013). Detecting offsets in GPS time series: First results from the detection of offsets in GPS experiment. *Journal of Geophysical Research: Solid Earth*, *118*(5), 2397–2407. doi: 10.1002/jgrb.50152

Ghosh, A., Becker, T. W., & Humphreys, E. D. (2013). Dynamics of the North American continent. *Geophysical Journal International*, *194*(2), 651–669. (Publisher: Oxford Academic) doi: 10.1093/gji/ggt151

Gourmelen, N., & Amelung, F. (2005). Postseismic Mantle Relaxation in the Central Nevada Seismic Belt. *Science*, *310*(5753), 1473–1476. doi: 10.1126/science.1119798

Haacker, E. M. K., Kendall, A. D., & Hyndman, D. W. (2016). Water Level Declines in the High Plains Aquifer: Predevelopment to Resource Senescence. *Groundwater*, *54*(2), 231–242. doi: 10.1111/gwat.12350

Hammond, W. C., Blewitt, G., & Kreemer, C. (2011). Block modeling of crustal deformation of the northern Walker Lane and Basin and Range from GPS velocities. *Journal of Geophysical Research: Solid Earth*, *116*(B4). doi: 10.1029/2010JB007817

Hammond, W. C., Blewitt, G., & Kreemer, C. (2016). GPS Imaging of vertical land motion in California and Nevada: Implications for Sierra Nevada uplift. *Journal of Geophysical Research: Solid Earth*, *121*(10), 7681–7703. doi: 10.1002/2016JB013458

Hammond, W. C., Kreemer, C., Zaliapin, I., & Blewitt, G. (2019). Drought-Triggered Magmatic Inflation, Crustal Strain, and Seismicity Near the Long Valley Caldera, Central Walker Lane. *Journal of Geophysical Research: Solid Earth*, *124*(6), 6072–6091. doi: 10.1029/2019JB017354

Hashima, A., & Sato, T. (2017). A megathrust earthquake cycle model for Northeast Japan: bridging the mismatch between geological uplift and geodetic subsidence. *Earth, Planets and Space*, *69*(1), 23. doi: 10.1186/s40623-017-0606-6

Hawkins, R., Husson, L., Choblet, G., Bodin, T., & Pfeffer, J. (2019). Virtual Tide Gauges for Predicting Relative Sea Level Rise. *Journal of Geophysical Research: Solid Earth*, *124*(12), 13367–13391. doi: 10.1029/2019JB017943

Hearn, E. H., Pollitz, F. F., Thatcher, W. R., & Onishi, C. T. (2013). How do "ghost transients" from past earthquakes affect GPS slip rate estimates on southern California faults? *Geochemistry, Geophysics, Geosystems*, *14*(4), 828–838. doi: 10.1002/ggge.20080

Herring, T. A., Melbourne, T. I., Murray, M. H., Floyd, M. A., Szeliga, W. M., King, R. W., … Wang, L. (2016). Plate Boundary Observatory and related networks: GPS data analysis methods and geodetic products. *Reviews of Geophysics*, *54*(4), 759–808. doi: 10.1002/2016RG000529

Hurwitz, S., & Lowenstern, J. B. (2014). Dynamics of the Yellowstone hydrothermal system. *Reviews of Geophysics*, *52*(3), 375–411. doi: 10.1002/2014RG000452

Husson, L., Bodin, T., Spada, G., Choblet, G., & Kreemer, C. (2018). Bayesian surface reconstruction of geodetic uplift rates: Mapping the global fingerprint of Glacial Isostatic Adjustment. *Journal of Geodynamics*, *122*, 25–40. doi: 10.1016/j.jog.2018.10.002

Johnson, K. M., & Tebo, D. (2018). Capturing 50 Years of Postseismic Mantle Flow at Nankai Subduction Zone. *Journal of Geophysical Research: Solid Earth*, *123*(11), 10,091–10,106. doi: 10.1029/2018JB016345

Jónsson, S., Zebker, H., Segall, P., & Amelung, F. (2002). Fault Slip Distribution of the 1999 Mw 7.1 Hector Mine, California, Earthquake, Estimated from Satellite Radar and GPS Measurements. *Bulletin of the Seismological Society of America*, *92*(4), 1377–1389. doi: 10.1785/0120000922

Kreemer, C., Blewitt, G., & Klein, E. C. (2014). A geodetic plate motion and Global Strain Rate Model. *Geochemistry, Geophysics, Geosystems*, *15*(10), 3849–3889. doi: 10.1002/2014GC005407

Kreemer, C., Hammond, W. C., & Blewitt, G. (2018). A Robust Estimation of the 3-D Intraplate Deformation of the North American Plate From GPS. *Journal of Geophysical Research: Solid Earth*, *123*(5), 4388–4412. doi: 10.1029/2017JB015257

Latychev, K., Mitrovica, J. X., Tamisiea, M. E., Tromp, J., Christara, C. C., & Moucha, R. (2005). GIA-induced secular variations in the Earth's long wavelength gravity field: Influence of 3-D viscosity variations. *Earth and Planetary Science Letters*, *240*(2), 322–327. doi: 10.1016/j.epsl.2005.10.001

Li, T., Wu, P., Wang, H., Steffen, H., Khan, N. S., Engelhart, S. E., . . . Horton, B. P. (2020). Uncertainties of Glacial Isostatic Adjustment Model Predictions in North America Associated With 3D Structure. *Geophysical Research Letters*, *47*(10), e2020GL087944. doi: 10.1029/2020GL087944

Liu, L., & Stegman, D. R. (2011). Segmentation of the Farallon slab. *Earth and Planetary Science Letters*, *311*(1), 1–10. doi: 10.1016/j.epsl.2011.09.027

Longuevergne, L., Scanlon, B. R., & Wilson, C. R. (2010). GRACE Hydrological estimates for small basins: Evaluating processing approaches on the High Plains Aquifer, USA. *Water Resources Research*, *46*(11). doi: 10.1029/2009WR008564

McCaffrey, R., Long, M. D., Goldfinger, C., Zwick, P. C., Nabelek, J. L., Johnson, C. K., & Smith, C. (2000). Rotation and plate locking at the Southern Cascadia Subduction Zone. *Geophysical Research Letters*, *27*(19), 3117–3120. doi: 10.1029/2000GL011768

Meade, B. J., & Hager, B. H. (2005). Block models of crustal motion in southern California constrained by GPS measurements. *Journal of Geophysical Research: Solid Earth*, *110*(B3). doi: 10.1029/2004JB003209

Montgomery-Brown, E. K., Wicks, C. W., Cervelli, P. F., Langbein, J. O., Svarc, J. L., Shelly, D. R., . . . Lisowski, M. (2015). Renewed inflation of Long Valley Caldera, California (2011 to 2014). *Geophysical Research Letters*, *42*(13), 5250–5257. doi: 10.1002/2015GL064338

Morton, R. A., Bernier, J. C., & Barras, J. A. (2006). Evidence of regional subsidence and associated interior wetland loss induced by hydrocarbon production, Gulf Coast region, USA. *Environmental Geology*, *50*(2), 261. doi: 10.1007/s00254-006-0207-3

Murray, J. R., Segall, P., Cervelli, P., Prescott, W., & Svarc, J. (2001). Inversion of GPS data for spatially variable slip-rate on the San Andreas Fault near Parkfield, CA. *Geophysical Research Letters*, *28*(2), 359–362. doi: 10.1029/2000GL011933

Murray, K. D., & Lohman, R. B. (2018). Short-lived pause in Central California subsidence after heavy winter precipitation of 2017. *Science Advances*, *4*(8), eaar8144. doi: 10.1126/sciadv.aar8144

Nakiboglu, S. M., & Lambeck, K. (1983). A reevaluation of the isostatic rebound of Lake Bonneville. *Journal of Geophysical Research: Solid Earth*, *88*(B12), 10439–10447. doi: 10.1029/JB088iB12p10439

National Research Council. (2012). *Sea-Level Rise for the Coasts of California, Oregon, and Washington: Past, Present, and Future.* doi: 10.17226/13389

Neely, W. R., Borsa, A. A., & Silverii, F. (2020). GInSAR: A cGPS Correction for Enhanced InSAR Time Series. *IEEE Transactions on Geoscience and Remote Sensing*, *58*(1), 136–146. doi: 10.1109/TGRS.2019.2934118

Nicot, J.-P., & Scanlon, B. R. (2012). Water Use for Shale-Gas Production in Texas, U.S. *Environmental Science & Technology*, *46*(6), 3580–3586. doi: 10.1021/es204602t

Page, E. S. (1954). Continuous inspection schemes. *Biometrika*, *41*(1-2), 100–115. doi: 10.1093/biomet/41.1-2.100

Park, K.-D., Nerem, R. S., Davis, J. L., Schenewerk, M. S., Milne, G. A., & Mitrovica, J. X. (2002). Investigation of glacial isostatic adjustment in the northeast U.S. using GPS measurements. *Geophysical Research Letters*, *29*(11), 4–1–4–4. doi: 10.1029/2001GL013782

Paulson, A., Zhong, S., & Wahr, J. (2007). Inference of mantle viscosity from GRACE and relative sea level data. *Geophysical Journal International*, *171*(2), 497–508. (Publisher: Oxford Academic) doi: 10.1111/j.1365-246X.2007.03556.x

Peltier, W. (1996). Global sea level rise and glacial isostatic adjustment: An analysis of data from the East Coast of North America. *Geophysical Research Letters*, *23*(7), 717–720. doi: 10.1029/96GL00848

Peltier, W. (2004). Global glacial isostsy and the surface of the ice-age Earth: the ICE-5G (VM2) model and GRACE. *Annual Review of Earth and Planetary Sciences*, *32*(1), 111–149. doi: 10.1146/annurev.earth.32.082503.144359

Peltier, W., & Andrews, J. T. (1976). Glacial-Isostatic Adjustment—I. The Forward Problem. *Geophysical Journal International*, *46*(3), 605–646. doi: 10.1111/j.1365-246X.1976.tb01251.x

Peltier, W., Argus, D. F., & Drummond, R. (2018). Comment on "An Assessment of the ICE-6G_c (VM5a) Glacial Isostatic Adjustment Model" by Purcell et al. *Journal of Geophysical Research: Solid Earth*, *123*(2), 2019–2028. doi: 10.1002/2016JB013844

Pollitz, F. F., Wicks, C., & Thatcher, W. (2001). Mantle Flow Beneath a Continental Strike-Slip Fault: Postseismic Deformation After the 1999 Hector Mine Earthquake. *Science*, *293*(5536), 1814–1818. doi: 10.1126/science.1061361

Powell, C. A., Bollinger, G. A., Chapman, M. C., Sibol, M. S., Johnston, A. C., & Wheeler, R. L. (1994). A Seismotectonic Model for the 300-Kilometer-Long Eastern Tennessee Seismic Zone. *Science*, *264*(5159), 686–688.

Rodell, M., Famiglietti, J. S., Wiese, D. N., Reager, J. T., Beaudoing, H. K., Landerer, F. W., & Lo, M.-H. (2018). Emerging trends in global freshwater availability. *Nature*, *557*(7707), 651–659. doi: 10.1038/s41586-018-0123-1

Rollins, C., Barbot, S., & Avouac, J.-P. (2015). Postseismic Deformation Following the 2010 M=7.2 El Mayor-Cucapah Earthquake: Observations, Kinematic Inversions, and Dynamic Models. *Pure and Applied Geophysics*, *172*(5), 1305–1358. doi: 10.1007/s00024-014-1005-6

Santamaría-Gómez, A., Bouin, M.-N., Collilieux, X., & Wöppelmann, G. (2011). Correlated errors in GPS position time series: Implications for velocity estimates. *Journal of Geophysical Research: Solid Earth*, *116*(B1). doi: 10.1029/2010JB007701

Save, H., Bettadpur, S., & Tapley, B. D. (2016). High-resolution CSR GRACE RL05 mascons. *Journal of Geophysical Research: Solid Earth*, *121*(10), 7547–7569. doi: 10.1002/2016JB013007

Schaeffer, A. J., & Lebedev, S. (2014). Imaging the North American continent using waveform inversion of global and USArray data. *Earth and Planetary Science Letters*, *402*, 26–41. doi: 10.1016/j.epsl.2014.05.014

Schmalzle, G. M., McCaffrey, R., & Creager, K. C. (2014). Central Cascadia subduction zone creep. *Geochemistry, Geophysics, Geosystems*, *15*(4), 1515–1532. doi: 10.1002/2013GC005172

Schmandt, B., & Lin, F.-C. (2014). P and S wave tomography of the mantle beneath the United States. *Geophysical Research Letters*, *41*(18), 6342–6349. doi: 10.1002/2014GL061231

Seager, R., Hoerling, M., Schubert, S., Wang, H., Lyon, B., Kumar, A., … Henderson, N. (2015). Causes of the 2011–14 California Drought. *Journal of Climate*, *28*(18), 6997–7024. doi: 10.1175/JCLI-D-14-00860.1

Sella, G. F., Stein, S., Dixon, T. H., Craymer, M., James, T. S., Mazzotti, S., & Dokka, R. K. (2007). Observation of glacial isostatic adjustment in "stable" North America with GPS. *Geophysical Research Letters*, *34*(2). doi: 10.1029/2006GL027081

Seneviratne, S. I., Viterbo, P., Lüthi, D., & Schär, C. (2004). Inferring Changes in Terrestrial Water Storage Using ERA-40 Reanalysis Data: The Mississippi River Basin. *Journal of Climate*, *17*(11), 2039–2057. doi: 10.1175/1520-0442(2004)017⟨2039:ICITWS⟩2.0.CO;2

Silverii, F., Montgomery-Brown, E. K., Borsa, A. A., & Barbour, A. J. (2020). Hydrologically Induced Deformation in Long Valley Caldera and Adjacent Sierra Nevada. *Journal of Geophysical Research: Solid Earth*, *125*(5), e2020JB019495. doi: 10.1029/2020JB019495

Simon, K. M., & Riva, R. E. M. (2020). Uncertainty Estimation in Regional Models of Long-Term GIA Uplift and Sea-level Change: An Overview. *Journal of Geophysical Research: Solid Earth*, *n/a*(n/a), e2019JB018983. doi: 10.1029/2019JB018983

Smith-Konter, B. R., Thornton, G. M., & Sandwell, D. T. (2014). Vertical crustal displacement due to interseismic deformation along the San Andreas fault: Constraints from tide gauges. *Geophysical Research Letters*, *41*(11), 3793–3801. doi: 10.1002/2014GL060091

Snay, R. A., Freymueller, J. T., Craymer, M. R., Pearson, C. F., & Saleh, J. (2016). Modeling 3-D crustal velocities in the United States and Canada. *Journal of Geophysical Research: Solid Earth*, *121*(7), 5365–5388. doi: 10.1002/2016JB012884

Snay, R. A., Saleh, J., & Pearson, C. F. (2018). Improving TRANS4D's model for vertical crustal velocities in Western CONUS. *Journal of Applied Geodesy*, *12*(3), 209–227. (Publisher: De Gruyter Section: Journal of Applied Geodesy) doi: 10.1515/jag-2018-0010

Tizzani, P., Battaglia, M., Castaldo, R., Pepe, A., Zeni, G., & Lanari, R. (2015). Magma and fluid migration at Yellowstone Caldera in the last three decades inferred from InSAR, leveling, and gravity measurements. *Journal of Geophysical Research: Solid Earth*, *120*(4), 2627–2647. doi: 10.1002/2014JB011502

Tregoning, P., Watson, C., Ramillien, G., McQueen, H., & Zhang, J. (2009). Detecting hydrologic deformation using GRACE and GPS. *Geophysical Research Letters*, *36*(15). doi: 10.1029/2009GL038718

Tuttle, M. P., Schweig, E. S., Sims, J. D., Lafferty, R. H., Wolf, L. W., & Haynes, M. L. (2002). The Earthquake Potential of the New Madrid Seismic Zone. *Bulletin of the Seismological Society of America*, *92*(6), 2080–2089. doi: 10.1785/0120010227

Törnqvist, T. E., Wallace, D. J., Storms, J. E. A., Wallinga, J., van Dam, R. L., Blaauw, M., … Snijders, E. M. A. (2008). Mississippi Delta subsidence primarily caused by compaction of Holocene strata. *Nature Geoscience*, *1*(3), 173–176. doi: 10.1038/ngeo129

van der Wal, W., Wu, P., Sideris, M. G., & Shum, C. K. (2008). Use of GRACE determined secular gravity rates for glacial isostatic adjustment studies in North-America. *Journal of Geodynamics*, *46*(3), 144–154. doi: 10.1016/j.jog.2008.03.007

Williams, S. D. P., Bock, Y., Fang, P., Jamason, P., Nikolaidis, R. M., Prawirodirdjo, L., … Johnson, D. J. (2004). Error analysis of continuous GPS position time series. *Journal of Geophysical Research: Solid Earth*, *109*(B3).

doi: 10.1029/2003JB002741

Wöppelmann, G., & Marcos, M. (2016). Vertical land motion as a key to understanding sea level change and variability. *Reviews of Geophysics*, *54*(1), 64–92. doi: 10.1002/2015RG000502

Yousefi, M., Milne, G., Li, S., Wang, K., & Bartholet, A. (2020). Constraining Interseismic Deformation of the Cascadia Subduction Zone: New Insights From Estimates of Vertical Land Motion Over Different Timescales. *Journal of Geophysical Research: Solid Earth*, *125*(3), e2019JB018248. doi: 10.1029/2019JB018248

Figure 1.

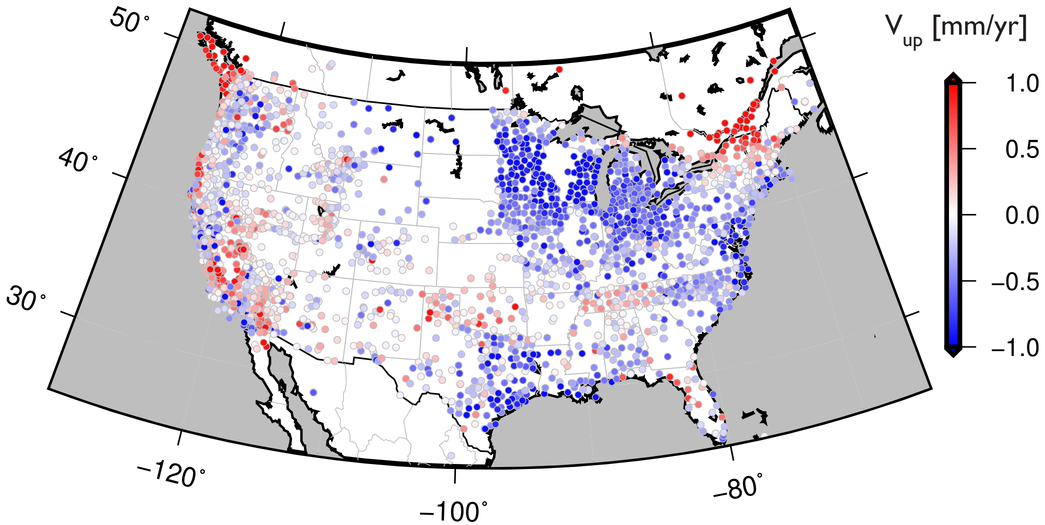

50°
40°
30°
−120°
−100°
−80°
V$_{up}$ [mm/yr]
1.0
0.5
0.0
−0.5
−1.0

Figure 2.

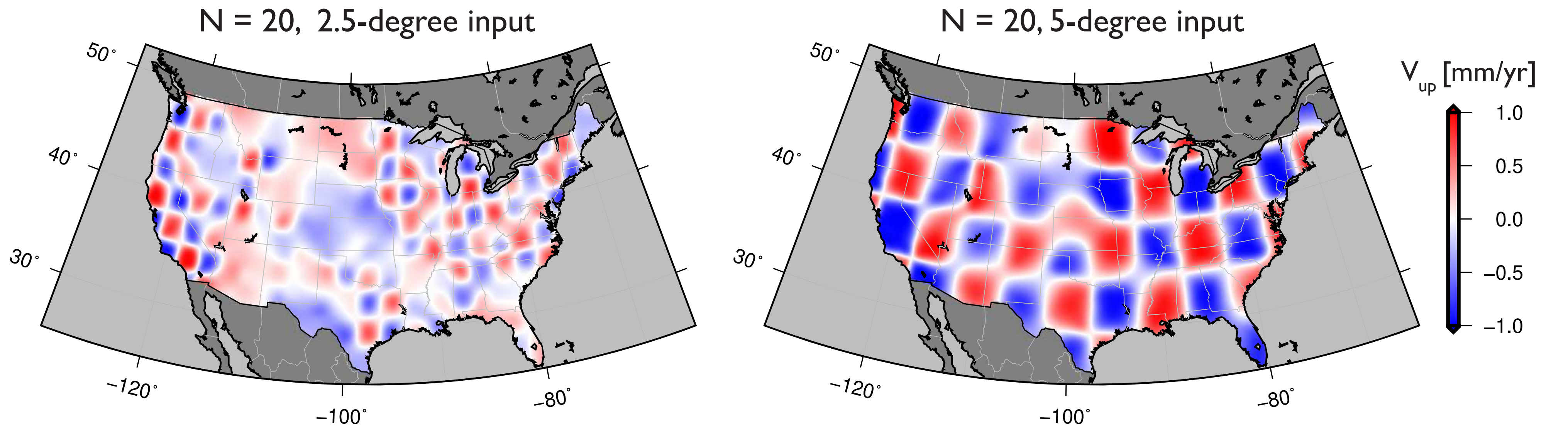
N = 20, 2.5-degree input
N = 20, 5-degree input
50°
40°
30°
−120°
−100°
−80°
V_{up} [mm/yr]
1.0
0.5
0.0
−0.5
−1.0

Figure 3.

a)

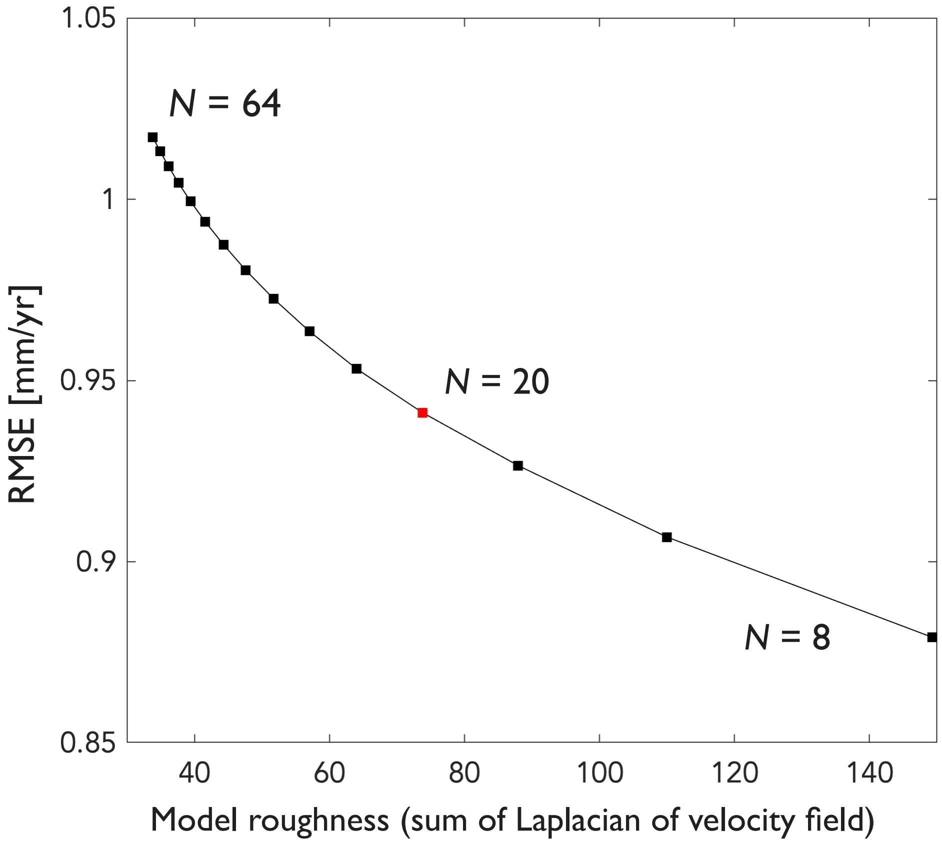

1.05
1
0.95
0.9
0.85
RMSE [mm/yr]
N = 64
N = 20
N = 8
40
60
80
100
120
140
Model roughness (sum of Laplacian of velocity field)

b)

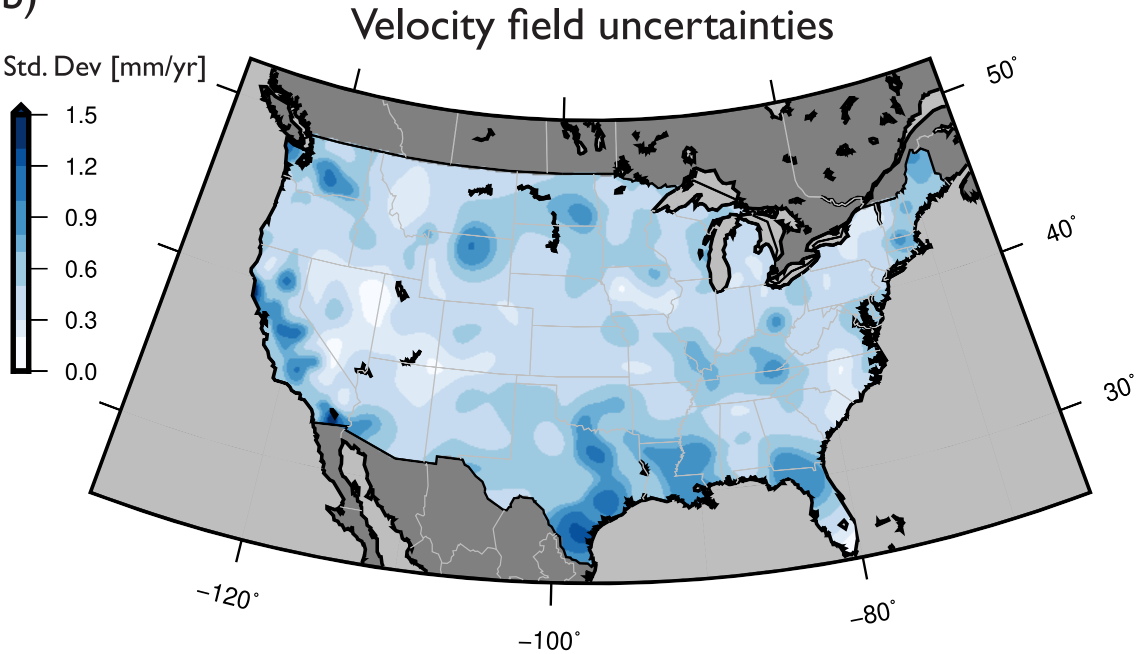

Velocity field uncertainties
Std. Dev [mm/yr]
1.5
1.2
0.9
0.6
0.3
0.0
50°
40°
30°
−120°
−100°
−80°

Figure 4.

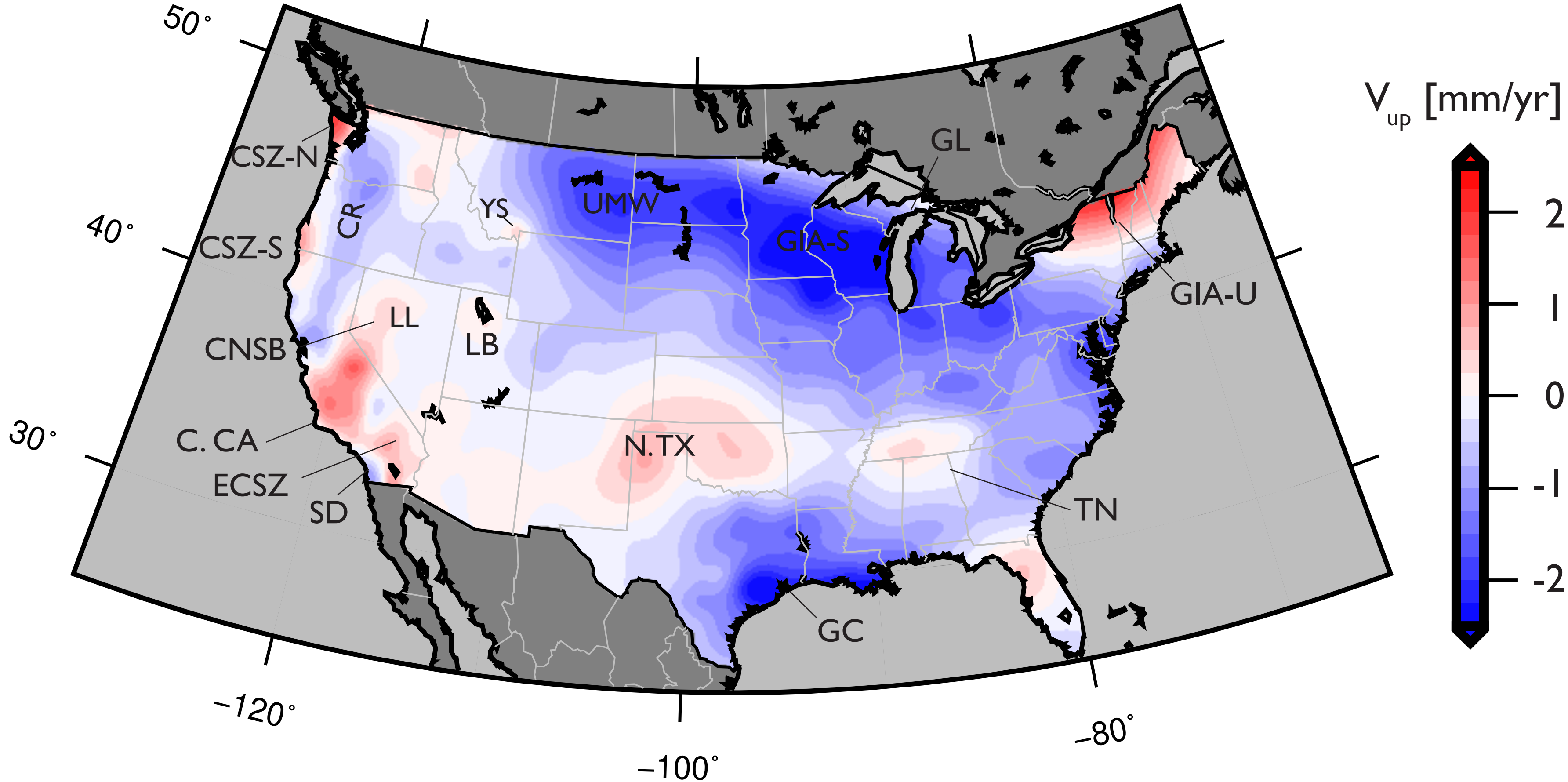

50°
40°
30°
−120°
−100°
−80°
CSZ-N
CSZ-S
CR
CNSB
C. CA
ECSZ
SD
LL
LB
YS
UMW
GIA-S
GL
GIA-U
N.TX
TN
GC
V_up [mm/yr]
2
1
0
-1
-2

Figure 5.

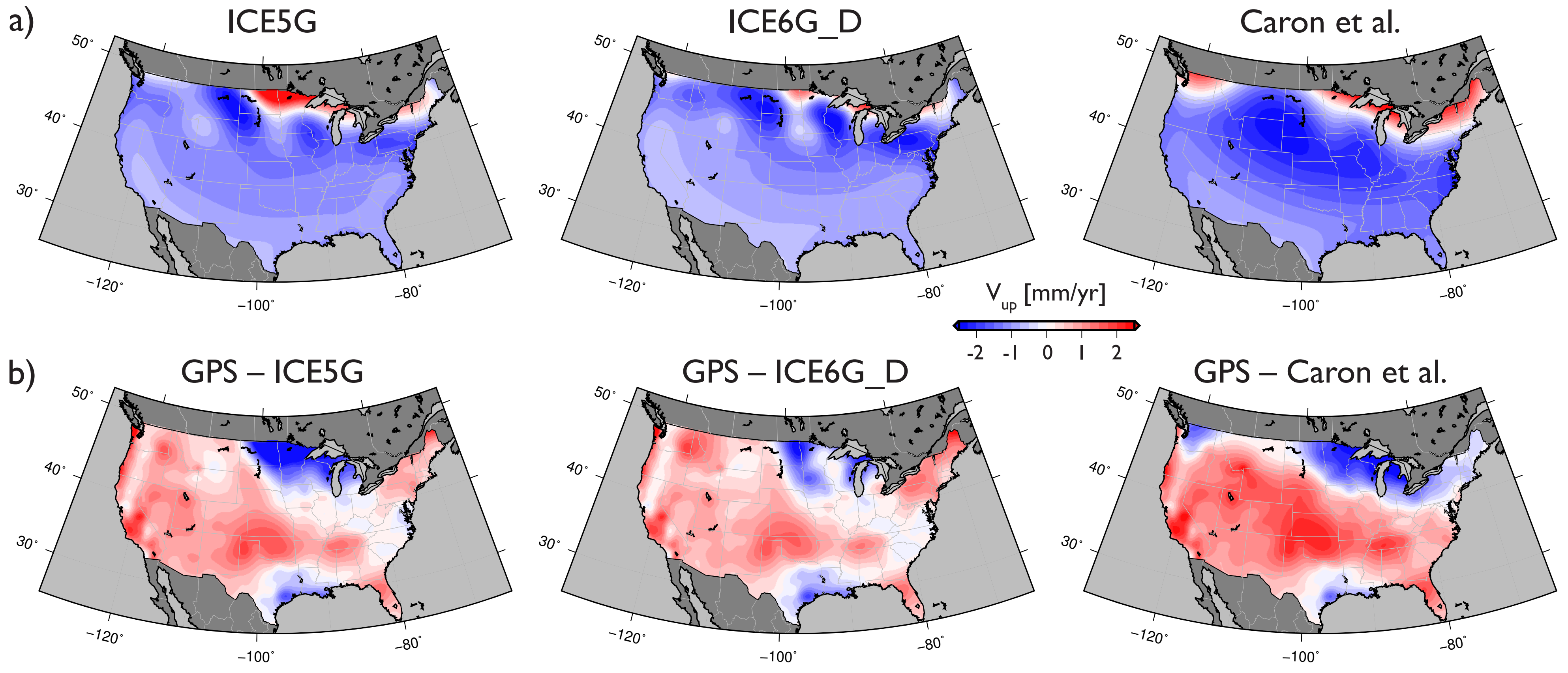
a)
ICE5G
ICE6G_D
Caron et al.
b)
GPS – ICE5G
GPS – ICE6G_D
GPS – Caron et al.
V_{up} [mm/yr]
-2 -1 0 1 2
50°
40°
30°
−120°
−100°
−80°

Figure 6.

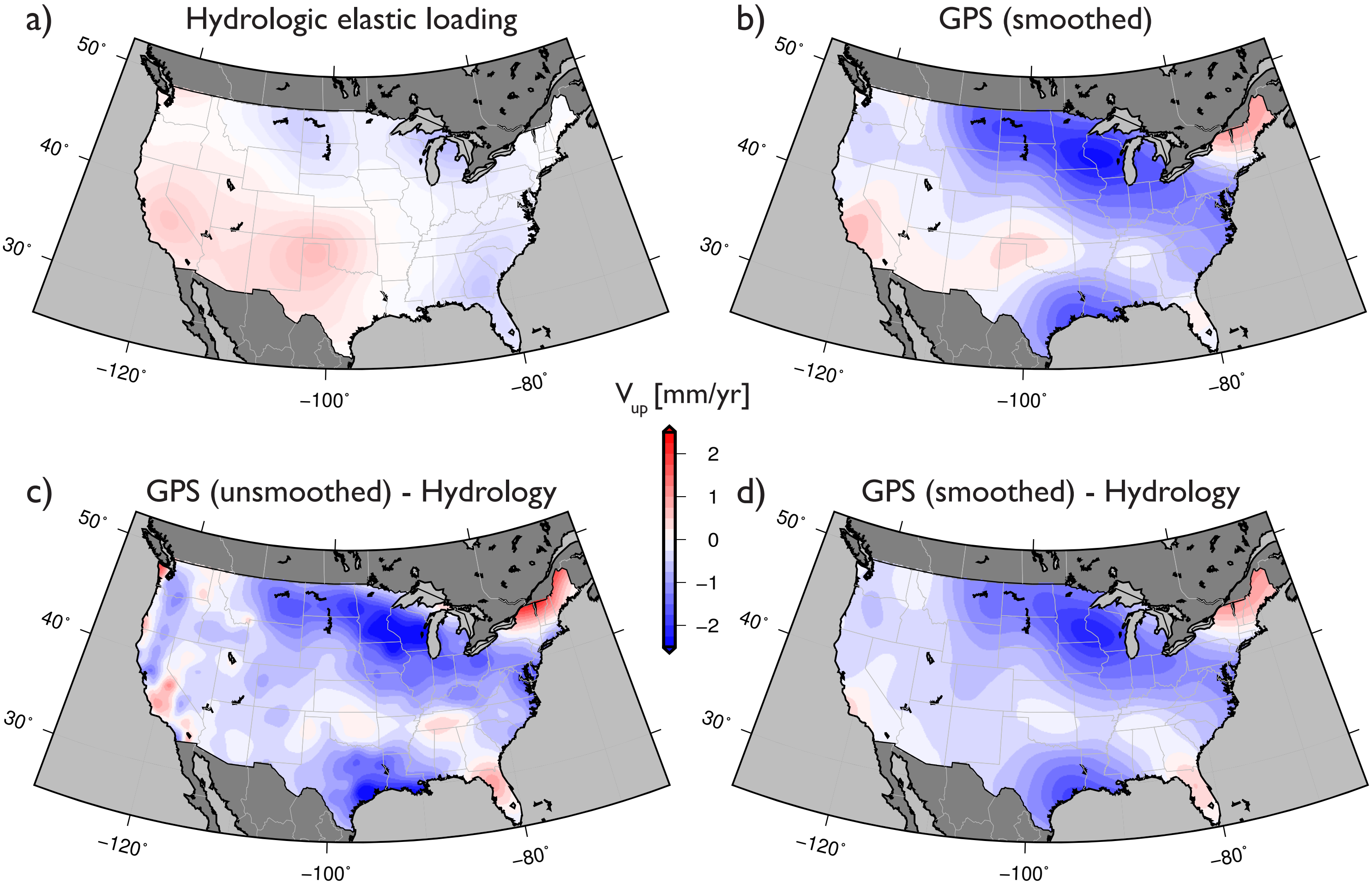
a)
Hydrologic elastic loading
b)
GPS (smoothed)
c)
GPS (unsmoothed) - Hydrology
d)
GPS (smoothed) - Hydrology
V_up [mm/yr]
2
1
0
−1
−2
50°
40°
30°
−120°
−100°
−80°

Figure 7.

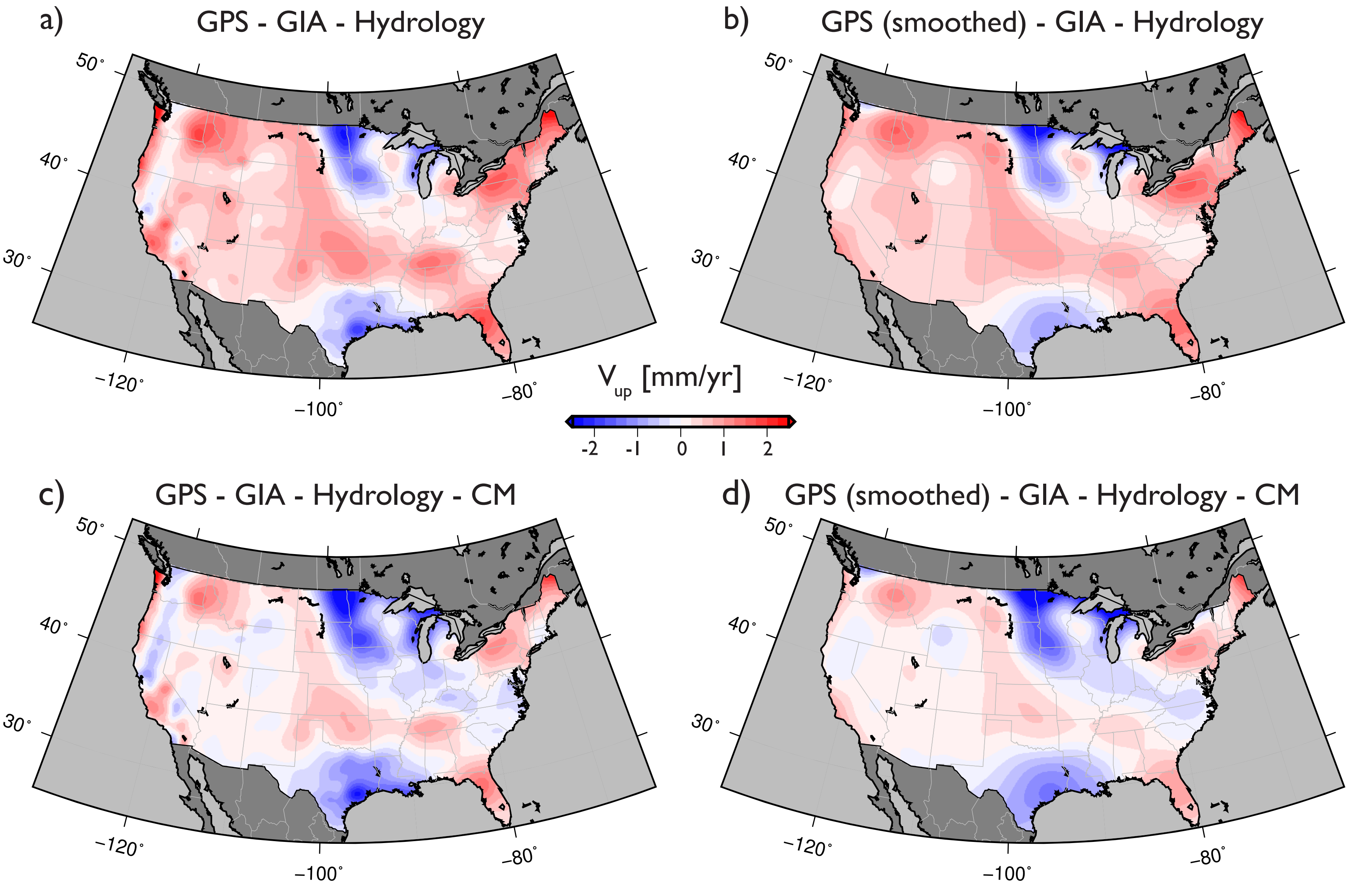
a) GPS - GIA - Hydrology
b) GPS (smoothed) - GIA - Hydrology
V_{up} [mm/yr]
-2
-1
0
1
2
c) GPS - GIA - Hydrology - CM
d) GPS (smoothed) - GIA - Hydrology - CM
50°
40°
30°
−120°
−100°
−80°

Figure 8.

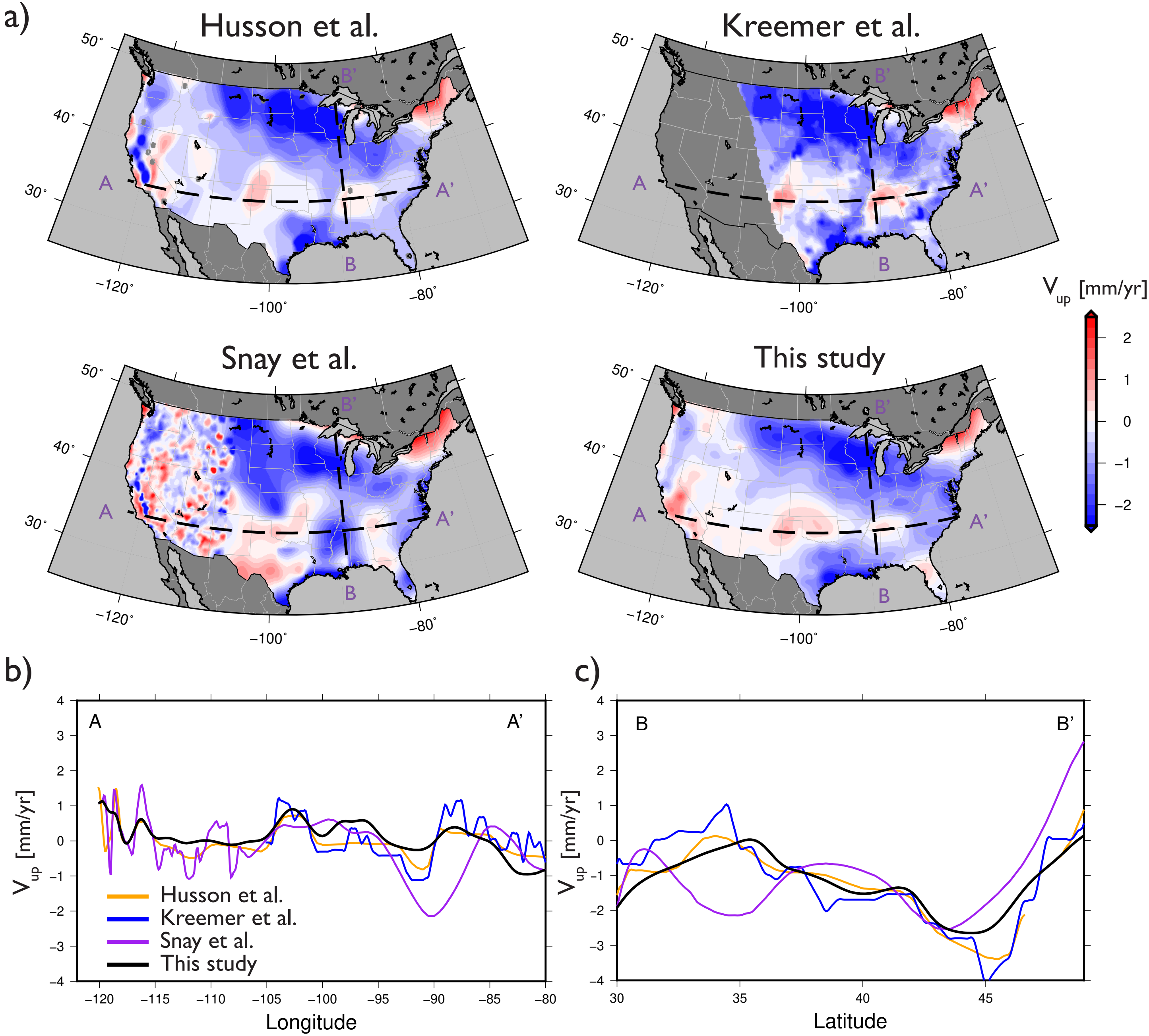

a)
Husson et al.
Kreemer et al.
Snay et al.
This study
A
A'
B
B'
50°
40°
30°
−120°
−100°
−80°
V_up [mm/yr]
2
1
0
−1
−2
b)
c)
Husson et al.
Kreemer et al.
Snay et al.
This study
V_up [mm/yr]
Longitude
Latitude